CACR-94-02

A Time-Dependent Numerical Code for Extended Boussinesq Equations

Ge Wei and James T. Kirby
Center for Applied Coastal Research
Department of Civil Engineering
University of Delaware
Newark, DE 19716

January, 1994

Abstract

A numerical code for the extended Boussinesq equations derived by Nwogu (1993) is developed. The model utilizes a fourth-order predictor-corrector method to advance in time, and discretizes first order spatial derivatives to fourth-order accuracy, thus reducing all truncation errors to a level smaller than the dispersive terms retained by the model. The basic numerical scheme is described, and we discuss unresolved issues pertaining to the application of boundary conditions. The model is applied to several examples of wave propagation in variable depth, and computed solutions are compared with experimental data. These initial results indicate that the model is capable of simulating wave transformation from relatively deep water to shallow water, giving accurate predictions of the height and shape of shoaled waves in both regular and irregular wave experiments.

Contents

List of Figures

1 Introduction

The ability to accurately predict wave transformation from deep to shallow water is vital to an understanding of coastal processes. As waves propagate toward shore, a combination of shoaling, refraction and diffraction effects modify the wave form. Nonlinear effects induce energy transfers both up and down the spectrum, leading to the generation of low-frequency surf-beat as well as high-frequency corrections (enhancements) to the shoaling wave crests.

Boussinesq-type equations, which include the lowest order effects of nonlinearity and frequency dispersion, have been shown to provide an accurate description of wave evolution in coastal regions, if used within the bounds of the validity of the underlying approximations. The first such set of equations for variable depth was derived by Peregrine (1967), and use the surface displacement η and a depth-averaged horizontal velocity $\overline{u}$ as dependent variables. Using frequency-domain formulations derived from Peregrine's equations, Freilich and Guza (1984) and Elgar and Guza (1985) have demonstrated that the evolution of power spectra of normally incident waves may be accurately predicted, while Elgar and Guza (1986) and Elgar et al (1990) have shown that the evolution of bispectra or third-moment statistics is also well predicted. The latter result amounts to a demonstration that the Boussinesq-type models are capable of predicting the shape of the underlying waves, which is quantified through accurate prediction of third-moment statistics for the surface displacement η and the Hilbert transform of η. Freilich et al (1993) provided evidence that the frequency domain model also correctly predicts the shoreward evolution of a directional wave train, using a parabolic equation method similar to that employed by Liu et al (1985).

Similar success has been noted in comparisons between laboratory data and model predictions. Goring (1978) has shown that the models give good predictions of the scattering and transmission of solitary waves at depth transitions, while Liu et al (1985) and Rygg (1988) have demonstrated that accurate predictions of wave refraction and focussing by underwater shoals may be made (Whalin, 1971). Kirby (1990) has shown that an angular spectrum formulation of the standard Boussinesq model gave good predictions of the evolution of a Mach stem measured in the laboratory (Hammack, Scheffner and Segur, 1990); this example is considered further below.

Due to increasing error in the modelled linear dispersion relation with increasing wa-

ter depth, the standard Boussinesq equations are limited to relatively shallow water. Recently, efforts have been made by a number of investigators to derive alternative forms of Boussinesq equations which can be applied in deeper water regions (Witting, 1984; Murray, 1989; Madsen et al., 1991; Nwogu, 1993). Of these models, the two by Madsen et al and Nwogu have generated the most interest. Each model is different in the form and arrangement of dispersive terms, but both lead to a dispersion relation which may be interpreted as being a Padé approximant of the full linear dispersion relation. This result is significant for two reasons. First, although the Boussinesq model equations are derived to provide a correction to $O(\mu^2)$ to the shallow water theory (where μ is essentially a scale for the value of kh), the property of the Padé approximant is such that the resulting dispersion relation may be interpreted as being accurate through $O(\mu^4)$. Secondly, the resulting approximation is almost guaranteed to be a more robust predictor of the correct result for large μ than corresponding Taylor series to $O(\mu^4)$ or, indeed, to much higher orders. Of these two models, the Boussinesq equations derived by Nwogu (1993) are obtained through a consistent derivation from the continuity and Euler equations of motion. In the derivation, the horizontal velocity at an arbitrary depth is used as the dependent variable. The depth at which the velocity is evaluated is then determined from the resulting dispersion relation compared with that of linear theory. As a result, the new form of equations are found to be able to predict the propagation of waves in water which is relatively much deeper than allowed by the standard approximation. (This increase in range of depths within which propagation may be accurately modelled should not be construed as a parallel claim to accuracy in prediction of water particle kinematics. Any Boussinesq-type approximation is going to be based on a vertical profile of horizontal velocity which is at most quadratic in z. This level of accuracy in representing the velocity profile will not be adequate in the deep water limit.)

In this study, we develop a high-order numerical model based on Nwogu's Boussinesq equations. We use a fourth-order predictor-corrector scheme for time stepping and discretize the first order spatial derivatives to fourth-order accuracy. This discretization automatically eliminates error terms which would be of the same form as the dispersive terms, and which must therefore be corrected for if lower order schemes are used. The model is applied to several cases of wave propagation from relatively deep to shallow water. Numerical results are compared with experimental data when available.

2 Governing Equations

The new form of Boussinesq equations derived by Nwogu (1993) are given by

$$\eta_t + \nabla \cdot [(h+\eta)\boldsymbol{u}] + \nabla \cdot \left\{ \left(\frac{{z_\alpha}^2}{2} - \frac{h^2}{6} \right) h \nabla(\nabla \cdot \boldsymbol{u}) + \left(z_\alpha + \frac{h}{2} \right) h \nabla[\nabla \cdot (h\boldsymbol{u})] \right\} = 0 \quad (1)$$

$$\boldsymbol{u}_t + g\nabla\eta + (\boldsymbol{u} \cdot \nabla)\boldsymbol{u} + z_\alpha \left\{ \frac{z_\alpha}{2} \nabla(\nabla \cdot \boldsymbol{u}_t) + \nabla[\nabla \cdot (h\boldsymbol{u}_t)] \right\} = 0 \quad (2)$$

where η is the surface elevation, h is the local water depth, $\boldsymbol{u} = (u, v)$ is the horizontal velocity at an arbitrary depth z_α, $\nabla = (\partial/\partial x, \partial/\partial y)$ is the horizontal gradiant operator, and g is the gravitational acceleration. The above equations are statements of conservation of mass and momentum, respectively. Compared to the standard Boussinesq equations derived by Peregrine (1967), there is an additional dispersive term in the continuity equation, and the coefficients of dispersive terms in the momentum equations are different. As will be shown below, it is these differences that improve the linear dispersive properties of the model and make the new form of equations usable in relatively deep water regions.

Consider the case of wave propagation in 1-D horizontal direction with constant depth. The equations then reduce to

$$\eta_t + hu_x + (\eta u)_x + (\alpha + 1/3)\, h^3 u_{xxx} = 0 \quad (3)$$

$$u_t + g\eta_x + uu_x + \alpha h^2 u_{txx} = 0 \quad (4)$$

where

$$\alpha = \frac{1}{2}\left(\frac{z_\alpha}{h}\right)^2 + \frac{z_\alpha}{h} \quad (5)$$

Linearizing the system of equations and substituting a trial solution

$$\eta = a\mathrm{e}^{i(kx-\omega t)}$$

$$u = u_0 \mathrm{e}^{i(kx-\omega t)} \quad (6)$$

leads to the linear dispersion relation

$$\omega^2 = gk^2 h \frac{[1 - (\alpha + 1/3)\,(kh)^2]}{1 - \alpha(kh)^2} \quad (7)$$

Figure 1 shows a comparison between the dispersion relation for full linear theory,

$$\omega^2 = gk \tanh kh \quad (8)$$

and the model dispersion relation for several values of α. The standard form of Boussinesq equations corresponds to the choice $\alpha = -1/3$. In the shallow water limit $kh \to 0$, all of the dispersion relations are asymptotically equivalent. However, in deep water regions where kh increases, the dispersion relation for arbitrary values of α deviates significantly from the linear theory.

The advantage of Nwogu's equations is that an optimized values of α can be determined such that the dispersion relation in a certain range of kh values is closest to the linear theory. A value of $\alpha = -4/10$ reduces (7) to the (2,2) Padé approximant of the exact relation (8), as shown by Witting (1984). The values of α may be further refined using an error minimizing criterion; Nwogu (1993) obtains a value of $\alpha = -0.390$ which corresponds to a depth of $z_\alpha = -0.531h$. As shown in Figure 1, the resulting dispersion relation is superior to the standard form of Boussinesq equation in the deep water limit. The actual value of α chosen will generally be a function of the range of kh values considered and the definition of the objective function defining the error estimate.

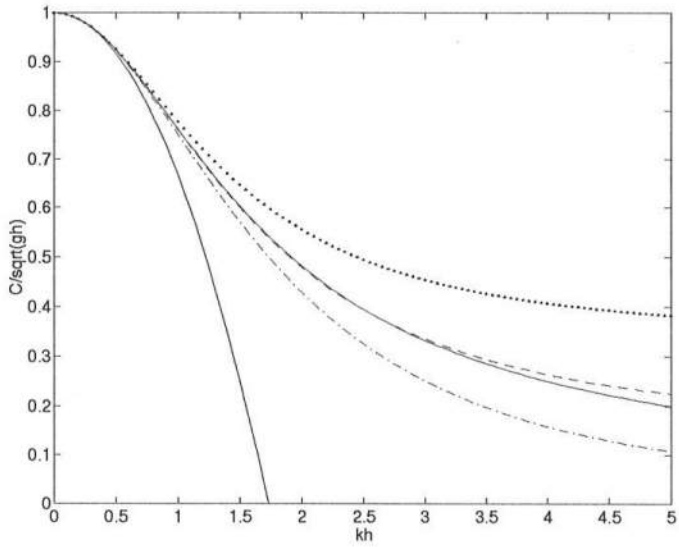

Figure 1: Comparison of dispersion relation for different values of α with linear theory: linear theory (——); $\alpha = -0.390$ (- - -); α=-0.400 ($\cdots$); α=-1/3 (- $\cdot$ - $\cdot$); α =0 (——).

3 Numerical Model

3.1 Predictor-corrector method

The choice of a numerical scheme for equations (1-2) is guided here by two principal factors. First, as occurs in any Boussinesq equation system, finite-differencing of first order derivative terms to second-order accuracy leads to leading order truncation error terms which are of the same form mathematically as the dispersive terms appearing in the model. These terms are eliminated consistently in the limit as $\Delta x, \Delta y, \Delta t \rightarrow 0$, but usually are large enough in magnitude to interfere with the solution at typical grid resolutions. Most existing schemes for equations of this type (Abbott et al, 1984; Nwogu, 1993) treat these terms by back substitution into the initial second-order accurate scheme, thus incorporating them as intentional distortions to the modelled dispersive effects. In this study, we seek, instead, to reduce all differencing errors to a size that is small relative to all retained terms in the model equations. We therefore adopt a scheme where the spatial differencing in first order terms is done to fourth-order accuracy, leading to a truncation error of $O(\Delta x^4/\mu^2)$ relative to the model dispersive terms at $O(\mu^2)$. In contrast, the dispersive terms themselves are finite-differenced only to second-order accuracy, leading to errors of $O(\Delta x^2)$ relative to the actual dispersive terms. Finally, the system of equations is written in a form that makes the application of a higher-order time-stepping procedure convenient. We utilize a fourth-order Adams predictor-corrector scheme to perform this updating.

The second factor is the impliciteness of the dispersive terms in the momentum equations. In order to address this, we rewrite (1-2) as

$$\eta_t = E(\eta, u, v) \tag{9}$$

$$U_t = F(\eta, u, v) + [F_1(v)]_t \tag{10}$$

$$V_t = G(\eta, u, v) + [G_1(u)]_t \tag{11}$$

where

$$U(u) = u + h\left[b_1 h u_{xx} + b_2 (hu)_{xx}\right] \tag{12}$$

$$V(v) = v + h\left[b_1 h v_{yy} + b_2 (hv)_{yy}\right] \tag{13}$$

are treated as simple variables in the time stepping scheme. The remaining quantities

E, F, G, F_1, G_1 are functions of η, u and v which are defined as

$$\begin{aligned} E(\eta,u,v) = & - [(h+\eta)u]_x - [(h+\eta)v]_y \\ & - \left\{a_1 h^3(u_{xx}+v_{xy}) + a_2 h^2\left[(hu)_{xx}+(hv)_{xy}\right]\right\}_x \\ & - \left\{a_1 h^3(v_{yy}+u_{xy}) + a_2 h^2\left[(hv)_{yy}+(hu)_{xy}\right]\right\}_y \end{aligned} \tag{14}$$

$$F(\eta,u,v) = - g\eta_x - (uu_x + vu_y) \tag{15}$$

$$G(\eta,u,v) = - g\eta_y - (vv_y + uv_x) \tag{16}$$

$$F_1(v) = - h\left[b_1 h v_{xy} + b_2 (hv)_{xy}\right] \tag{17}$$

$$G_1(u) = - h\left[b_1 h u_{xy} + b_2 (hu)_{xy}\right] \tag{18}$$

The constants a_1, a_2, b_1, b_2 are given by

$$a_1 = \beta^2/2 - 1/6, \quad a_2 = \beta + 1/2, \quad b_1 = \beta^2/2, \quad b_2 = \beta \tag{19}$$

where $\beta = z_\alpha/h$. For the standard form of the Boussinesq equations, the constants reduce to

$$a_1 = 0, \quad a_2 = 0, \quad b_1 = 1/6, \quad b_2 = -1/2 \tag{20}$$

The reason for isolating the time derivative of cross-differentiated terms on the right-hand side in (10-11) is to make the remaining left hand sides in U and V purely tridiagonal in form when we revert to the actual unknowns u and v and finite-difference dispersive terms to second-order accuracy. The resulting set of equations are then solved by sweeping each one in its own direction. The cross-derivative terms are evaluated using second-order extrapolation in the predictor step and second order iteration in the corrector step.

The governing equations are finite-differenced on an un-staggered grid in x, y, t. We discretize the independent variables as $x = i\Delta x, y = j\Delta y, t = n\Delta t$. Level n refers to information at the present, known time level. The predictor step is the third-order explicit Adams-Bashforth scheme, given by

$$\eta_{i,j}^{n+1} = \eta_{i,j}^n + \frac{\Delta t}{12}\left[23E_{i,j}^n - 16E_{i,j}^{n-1} + 5E_{i,j}^{n-2}\right] \tag{21}$$

$$\begin{aligned} U_{i,j}^{n+1} = U_{i,j}^n & + \frac{\Delta t}{12}\left[23F_{i,j}^n - 16F_{i,j}^{n-1} + 5F_{i,j}^{n-2}\right] \\ & + 2F_1^n - 3F_1^{n-1} + F_1^{n-2} \end{aligned} \tag{22}$$

$$\begin{aligned} V_{i,j}^{n+1} = V_{i,j}^n & + \frac{\Delta t}{12}\left[23G_{i,j}^n - 16G_{i,j}^{n-1} + 5G_{i,j}^{n-2}\right] \\ & + 2G_1^n - 3G_1^{n-1} + G_1^{n-2} \end{aligned} \tag{23}$$

where all information on the right is known from previous calculations. The values of $\eta_{i,j}^{n+1}$ are straightforward to obtain. The evaluation of horizontal velocities at the new time level, however, requires solution of tridiagonal systems which are linear in the unknowns at level $n+1$. Specifically, for a given j, $u_{i,j}^{n+1}(i = 1, 2, ..., M)$ are obtained through tridiagonal matrix solution. Similarly, $v_{i,j}^{n+1}(j = 1, 2, ..., N)$ are solved by a system of tridiagonal matrix equation for given i. The matrices involved are constant in time and may be pre-factored, inverted and stored for use at each time step.

After the predicted values of $\eta_{i,j}^{n+1}, u_{i,j}^{n+1}$ and $v_{i,j}^{n+1}$ are evaluated, we obtain the corresponding spatial derivatives $E_{i,j}^{n+1}, F_{i,j}^{n+1}, G_{i,j}^{n+1}, (F_1)_{i,j}^{n+1}, (G_1)_{i,j}^{n+1}$ from equations (14-18).

The corrector scheme is the fourth-order Adams-Moulton method, given by

$$\eta_{i,j}^{n+1} = \eta_{i,j}^{n} + \frac{\Delta t}{24}\left[9E_{i,j}^{n+1} + 19E_{i,j}^{n} - 5E_{i,j}^{n-1} + E_{i,j}^{n-2}\right] \tag{24}$$

$$U_{i,j}^{n+1} = U_{i,j}^{n} + \frac{\Delta t}{24}\left[9F_{i,j}^{n+1} + 19F_{i,j}^{n} - 5F_{i,j}^{n-1} + F_{i,j}^{n-2}\right] + F_1^{n+1} - F_1^{n} \tag{25}$$

$$V_{i,j}^{n+1} = V_{i,j}^{n} + \frac{\Delta t}{24}\left[9G_{i,j}^{n+1} + 19G_{i,j}^{n} - 5G_{i,j}^{n-1} + G_{i,j}^{n-2}\right] + G_1^{n+1} - G_1^{n} \tag{26}$$

The corrector step is iterated until the error between two successive results reaches a required limit. The error is computed for each of the three dependent variables η, u, v and is defined as

$$\Delta f = \frac{\sum_{i,j} |f_{i,j}^{n+1} - f_{i,j}^{(n+1)*}|}{\sum_{i,j} |f_{i,j}^{n+1}|} \tag{27}$$

where f denotes any of the variables and $()^*$ denotes the previous estimate. The corrector step is iterated if any of the Δf's exceeds 0.001. The scheme typically requires no iteration unless problems arise at boundaries.

Then the same procedure is applied to the next time step. Figure 2 shows the flow chart for the main computer program of the numerical model. Notation for the grid geometry is shown in Figure 3.

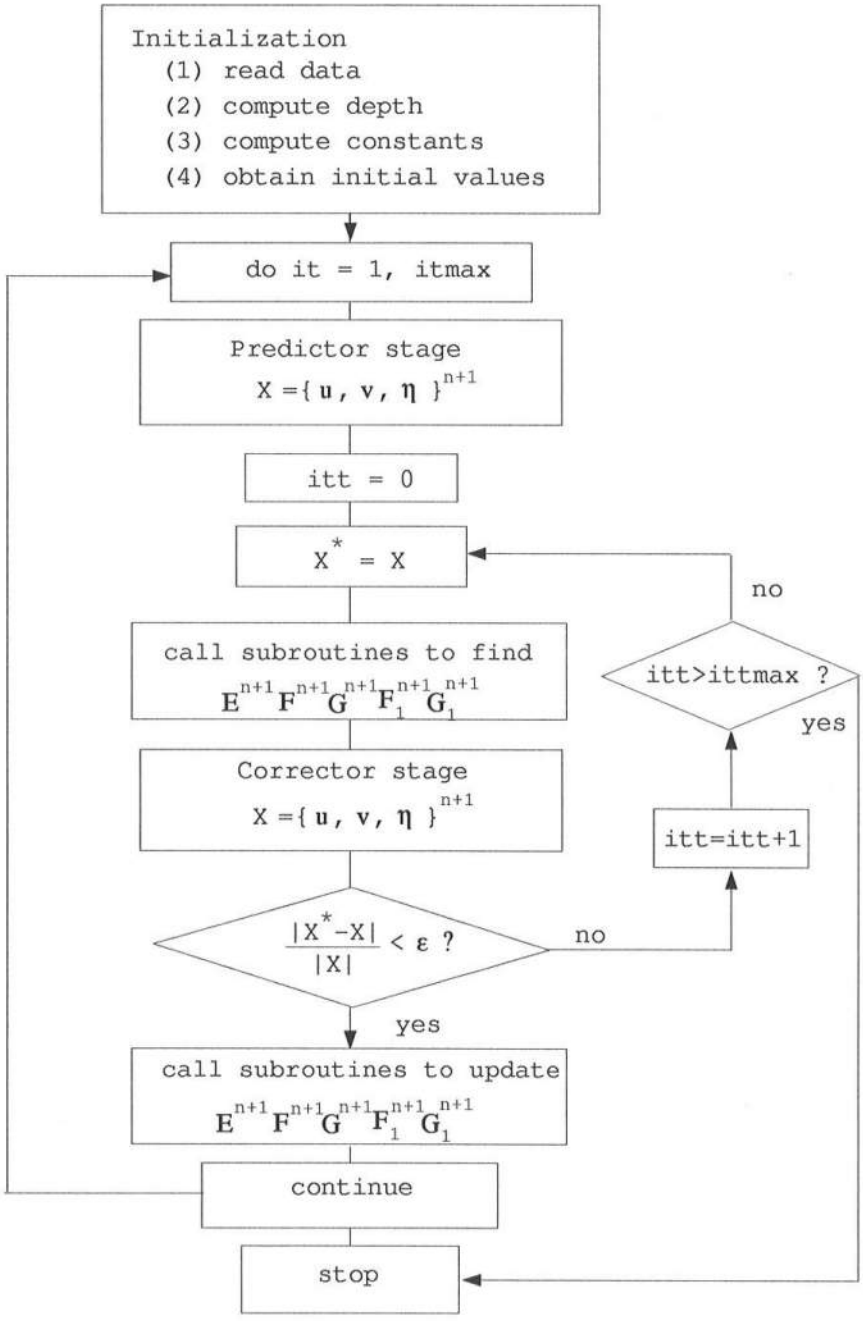

Figure 2: Flow chart of main computer program.

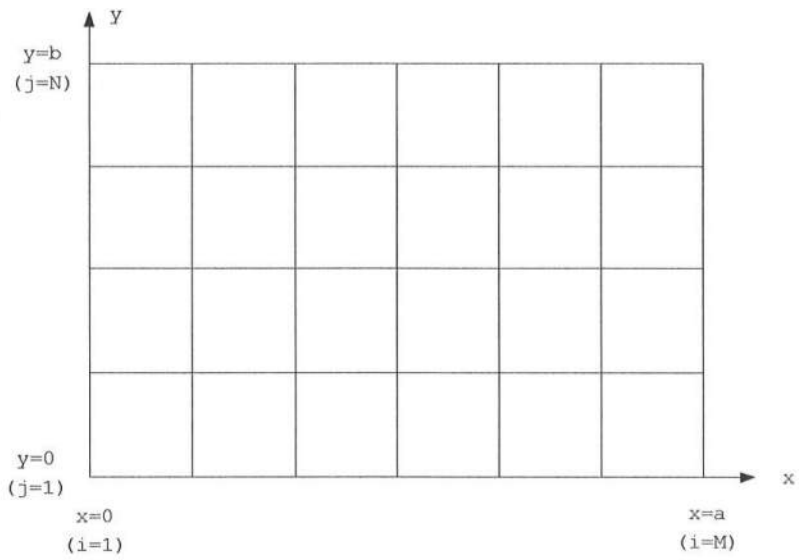

Figure 3: Definition of computational domain and boundaries.

3.2 Boundary conditions

Appropriate boundary conditions are needed for the numerical model to run properly. The examples shown below involve three types of lateral boundaries, which are discussed here in sequence. These are:

1. Impermeable, reflective vertical walls
2. Incident wave (or wavemaker) boundaries
3. Transmitting or absorbing boundaries

3.2.1 Reflective boundaries

For a general reflective boundary with an outward normal vector $\mathbf{n}$, we would anticipate on physical grounds that the kinematic boundary condition would be completely specified by the statement

$$\boldsymbol{u} \cdot \mathbf{n} = 0; \qquad \mathbf{x} \in \partial\Omega \tag{28}$$

where Ω is the fluid domain, $\partial\Omega$ is the boundary, and $\mathbf{x}$ is a position in the domain. Unfortunately, owing to the definition of $\boldsymbol{u}$, this is apparently not a complete statement. Consider (1) written as

$$\eta_t + \nabla \cdot \mathbf{M} = 0 \tag{29}$$

where

$$\mathbf{M} = (h+\eta)\boldsymbol{u} + \left(\frac{{z_\alpha}^2}{2} - \frac{h^2}{6}\right) h\nabla(\nabla \cdot \boldsymbol{u}) + \left(z_\alpha + \frac{h}{2}\right) h\nabla[\nabla \cdot (h\boldsymbol{u})] \tag{30}$$

is the volume flux vector. We may integrate (29) over Ω to obtain the result

$$\frac{dm}{dt} = -\int_{\partial\Omega} \mathbf{M} \cdot \mathbf{n} dS \tag{31}$$

where

$$m = \int_\Omega \eta dA \tag{32}$$

is the total excess volume in the domain. If the domain is completely enclosed by impermeable walls, we require that the rate of change of the excess volume be zero. This requirement is then satisfied by the condition

$$\mathbf{M} \cdot \mathbf{n} = 0; \qquad \mathbf{x} \in \partial\Omega \tag{33}$$

which is more complicated than (28). Consider, for example, the case of a wall parallel to the y-axis fronted by a region of constant depth h, for which the boundary condition becomes $M_x = 0$ or

$$(h+\eta)u + h^3(\alpha + \frac{1}{3})[u_{xx} + v_{xy}] = 0 \tag{34}$$

Setting $u = 0$ only covers a portion of the condition. If we consider the leading order terms in the mass conservation equation, however, we have

$$\eta_t + hu_x + hv_y = 0 \tag{35}$$

This may be differentiated with respect to x to obtain

$$(\eta_x)_t + h[u_{xx} + v_{xy}] = 0 \tag{36}$$

From (36), it is clear that the overall boundary condition is satisfied by additionally imposing

$$\nabla\eta \cdot \mathbf{n} = 0; \qquad \mathbf{x} \in \partial\Omega \tag{37}$$

which is consistent with the usual physical notion of total reflection at a vertical barrier. Finally, for the velocity component u_T tangent to the boundary, we require

$$\frac{\partial u_T}{\partial n} = 0; \qquad \mathbf{x} \in \partial\Omega \tag{38}$$

This last condition essentially imposes a no-shear condition for the flow along the bounding wall, which is not inconsistant with the inviscid flow being considered. This last condition would not seem to be required by the kinematic constraints on the system, but it has been used repeatedly in the literature (for example, Rygg (1988)), and we have not been able to stabilize the computational scheme without imposing it. This point requires further research, and is considered to be unresolved at present.

3.2.2 Wavemaker boundaries

For the examples considered below, we impose wavemaker boundary conditions by specifying the entire signal η, u, v on the boundary. This step does not allow for treatment of reflected waves arriving at the boundary, but has been seen to be adequate for the cases under study. The entire question of well - posedness of the incident wave boundary condition is being considered separately, and we are additionally considering approximate treatments of the boundary along the lines of the internal source functions of Larsen and Dancy (1983).

If incident wave elevation η_I is given (as in the example in section 4.4) and the wave height is small compared to the water depth, then we can use linear theory to obtain the incident wave velocity:

$$u_I = \frac{\omega}{kh_0[1-(\alpha+1/3)(kh_0)^2]}\eta_I \cos\theta \tag{39}$$

$$v_I = \frac{\omega}{kh_0[1-(\alpha+1/3)(kh_0)^2]}\eta_I \sin\theta \tag{40}$$

where k is the wavenumber, h_0 is the water depth and θ is the angle of wave propagation relative to the x-axis.

3.2.3 Absorbing boundaries

The final type of boundary in the present examples is the radiating or open boundary, which should absorb all energy arriving at the boundary from within the fluid domain. Treatment of this boundary is a problem of major interest in the modelling community, and we utilize some fairly well established techniques for the cases considered here.

A perfect radiation boundary should not allow wave reflection to occur. For the case where the wave phase speed c and the propagation direction θ at the boundary are known, the radiation condition is

$$\eta_t + c\cos\theta\eta_x = 0 \tag{41}$$

However, the present model is essentially dispersive, and so no single phase speed c exists which fully characterizes the system. Further, in two-dimensional applications, the wave direction θ is generally not known *a priori*. To solve the second problem, approximations to the perfect radiation condition are made. For wave propagation with the principle propagation direction close to the x-axis, the approximate radiation boundary condition can be written as (Engquist and Majda, 1977)

$$\eta_{tt} + c\eta_{xt} - \frac{c^2}{2}\eta_{yy} = 0 \tag{42}$$

which corresponds to the imposition of a parabolic approximation on the outgoing wave. To treat the first problem, phase speed c is specified by the long wave limit $c = \sqrt{gh}$.

The above approximate radiation condition inevitably introduces wave reflection along the boundaries and can eventually cause the model to blow up. To reduce the reflection, a damping layer is applied to the computing domain. Damping terms are added to the momentum equations as

$$U_t = F(\eta, u, v) + [F_1(v)]_t - w_1(x)u - w_2(x)(u_{xx} + u_{yy}) \tag{43}$$

$$V_t = G(\eta, u, v) + [G_1(u)]_t - w_1(x)v - w_2(x)(v_{xx} + v_{yy}) \tag{44}$$

where the damping terms with u and v are call "Newtonian cooling" and those with second order derivative are analogous to linear viscous terms in Navier-Stokes equations (Israeli and Orszag, 1981). The damping coefficients $w_1(x)$ and $w_2(x)$ are defined

as

$$w_1(x) = \begin{cases} 0 & ; \quad x < x_s \\ \alpha_1 \omega f(x) & ; \quad x > x_s \end{cases} \tag{45}$$

$$w_2(x) = \begin{cases} 0 & ; \quad x < x_s \\ \alpha_2 \nu f(x) & ; \quad x > x_s \end{cases} \tag{46}$$

where α_1 and α_2 are constants to be determined for the specific running, ω is the frequency of wave to be damped, x_s the starting coordinate of damping layer (the computing domain is from $x = 0$ to $x = x_l$), ν the viscous coefficient, and $f(x)$ is expressed as

$$f(x) = \frac{\exp(\frac{x-x_s}{x_l-x_s})^n - 1}{\exp(1) - 1} \tag{47}$$

The width of the damping layer (*i.e.* $x_l - x_s$) is usually taken to be two or three times the wave length. Numerical experiments show that the addition of damping layer combined with radiation boundary conditions works much better than radiation conditions alone.

4 Case studies

Both 1-D and 2-D versions of the numerical model described above have been developed and applied to a number of cases of wave propagation. For the 1-D model, we first investigate solitary wave propagation over a very long and flat bottom. Then, we study solitary wave shoaling on a slope, and compare the present results to results obtained using a boundary element model (Grilli et al, 1989). To further verify the model, we then study solitary wave reflection and random wave evolution on a slope and compare our results with experimental data. For 2-D version of the model, we first study wave evolution in a closed basin to verify symmetry of computed results and to test various boundary conditions. Then, the model is applied to simulate monochromatic wave propagation over an elliptic shoal and to study cnoidal wave reflection from the side wall in a rectangular wave basin. Comparisons of numerical solutions and experiment data are presented. The results show that the model is capable of simulating wave propagation over a wide range of water depths.

4.1 Solitary wave propagation over a flat bottom

The propagation of a solitary wave over a long distance provides a good test of the stability and conservative properties of the basic numerical scheme. In order to apply this test, we first need a solitary wave solution for Nwogu's model equations. Schember (1982) has described a method for obtaining approximate analytical solutions for solitary waves, using the standard Boussinesq approximation with depth averaged velocities. First, an approximate ordinary differential equation (to the same order of accuracy as the Boussinesq equations) for wave potential ϕ was obtained from the original coupled equations. The equation of ϕ is a fourth-order nonlinear ordinary differential equation which admits a closed-form solution, from which the horizontal velocity u and surface elevation η can be determined. Following the same procedure, we can obtain an analytical solution for the extended Boussinesq equations. Details of the derivation are included in Appendix A. The horizontal velocity u and surface elevation η of a solitary wave are found to be

$$u = A\text{sech}^2[B(x - Ct)] \tag{48}$$

$$\eta = A_1\text{sech}^2[B(x - Ct)] + A_2\text{sech}^4[B(x - Ct)] \tag{49}$$

where A, B, A_1, A_2 are constants which are defined as:

$$A = \frac{C^2 - gh}{C} \tag{50}$$

$$B = \left(\frac{C^2 - gh}{4h^2[(\alpha + 1/3)gh - \alpha C^2]} \right)^{1/2} \tag{51}$$

$$A_1 = \frac{C^2 - gh}{3[(\alpha + 1/3)gh - \alpha C^2]} h \tag{52}$$

$$A_2 = -\frac{(C^2 - gh)^2}{2ghC^2} \frac{[(\alpha + 1/3)gh + 2\alpha C^2]}{[(\alpha + 1/3)gh - \alpha C^2]} h \tag{53}$$

and where h is the water depth, g is the gravitational acceleration, and α is the parameter defined in (5). The phase speed C depends on the α value and the ratio of wave amplitude a to the water depth h ($\varepsilon = a/h$) through

$$2\alpha(\frac{C^2}{gh})^3 - (3\alpha + 1/3 + 2\alpha\varepsilon)(\frac{C^2}{gh})^2 + 2\varepsilon(\alpha + 1/3)(\frac{C^2}{gh}) + \alpha + 1/3 = 0 \tag{54}$$

which must be solved numerically. The analytical solution is used to specify the incident wave boundary condition for the numerical model.

The model was used to investigate solitary wave propagation in constant water depth of $0.45m$ over a horizontal distance of $450m$. Figure 4(a) shows the spatial variations of a solitary wave with amplitude $0.045m$ ($\epsilon = 0.1$) at various time steps. The results indicate that the initial wave pulses specified according to the theory in (48)-(54) undergo evolution at the start of the wave channel, with the result that a slightly higher solitary wave is formed together with a small dispersive tail. The amplitude of the tail and the initial deviation in solitary wave height both increase with increasing initial wave height. This result is partially due to the fact that the fourth order equation used to develop the analytical solution is only asymptotically equivalent to the model being solved numerically, so that the wave being input at the boundary of the numerical model does not correspond exactly to a solitary wave form as predicted by the model. Figure 4(b) shows a blow up of a wave with an initial amplitude of $0.135m$ ($\epsilon = 0.3$), with the solitary wave crests clipped off and the dispersive tail accentuated. The dispersive tail is seen to lag behind the evolved solitary wave, and shows a distinct ordering with low frequency waves near the front of the wave train and high frequency waves near the back, as would be expected for any dispersive wave train.

The amplitude variations of three solitary waves (amplitudes as $0.045m$, $0.090m$ and

$0.135m$) are shown in Figure 5. In Figure 6, the shapes of these solitary waves at times $t = 40s$ and $t = 160s$ are compared in detail. The important feature of the numerical solution is that the solitary wave which evolves out of the initial wave form then propagates for a long distance (at least 1000 water depths) without undergoing any additional damping or evolution. This indicates that the numerical code is free of unwanted dissipative effects, which would gradually damage the solitary wave form. Figure 5 shows that the solitary wave height predicted by the model is quite stable. Similar results were obtained for the mass contained in the solitary wave.

In Figure 6, solitary wave forms are compared at two widely separated instants in time. The two wave forms are translated by an amount predicted by the analytical phase speed C. The figure indicates that the numerically predicted phase speed is somewhat smaller than the analytically predicted one, and that the difference increases with increasing wave height.

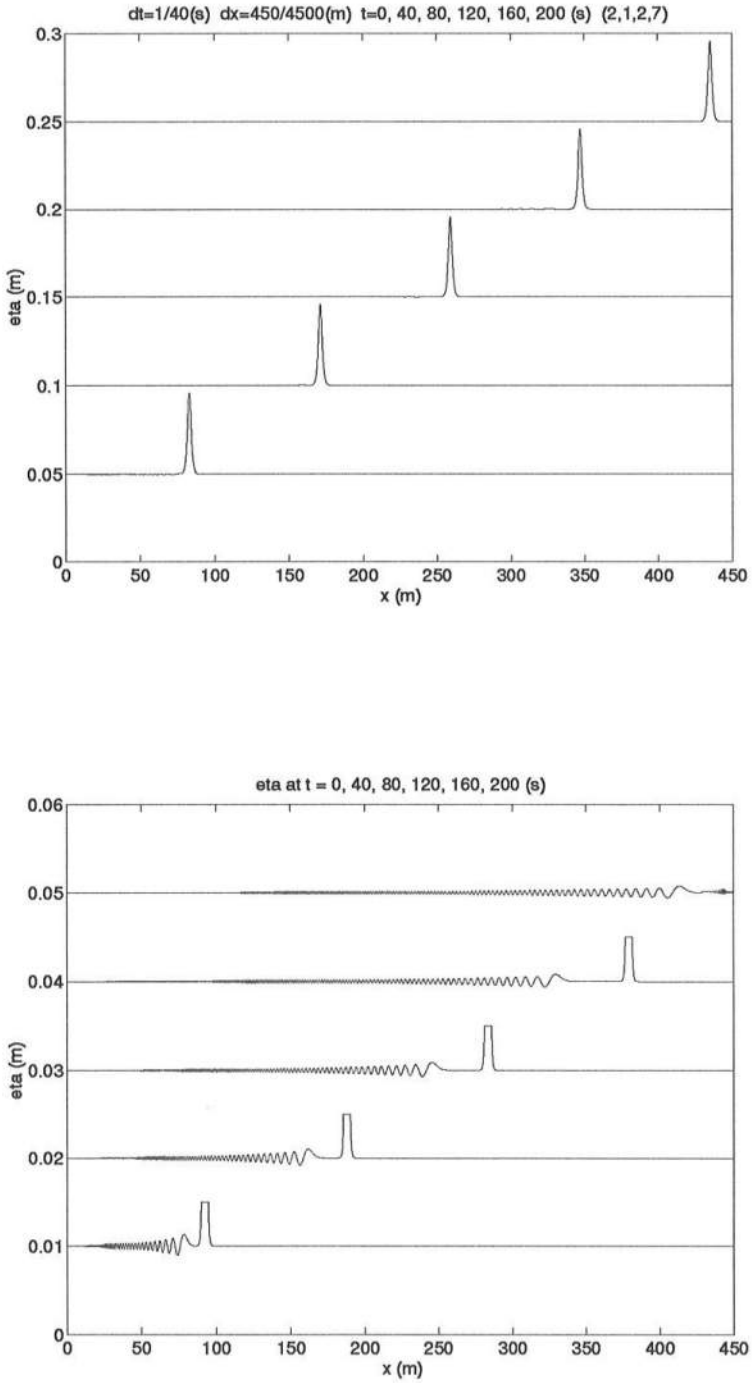

Figure 4: Spatial profiles of solitary wave with $\epsilon = 0.1$ (top) and $\epsilon = 0.3$ (bottom) evolving in water of constant depth ($h = 0.45m$).

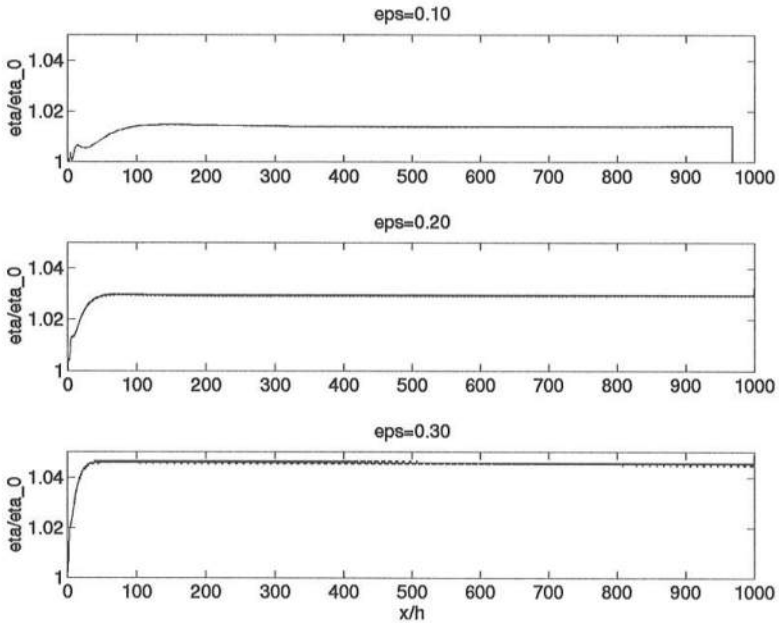

Figure 5: Amplitude variation of solitary waves for $\epsilon = 0.1, 0.2, 0.3$.

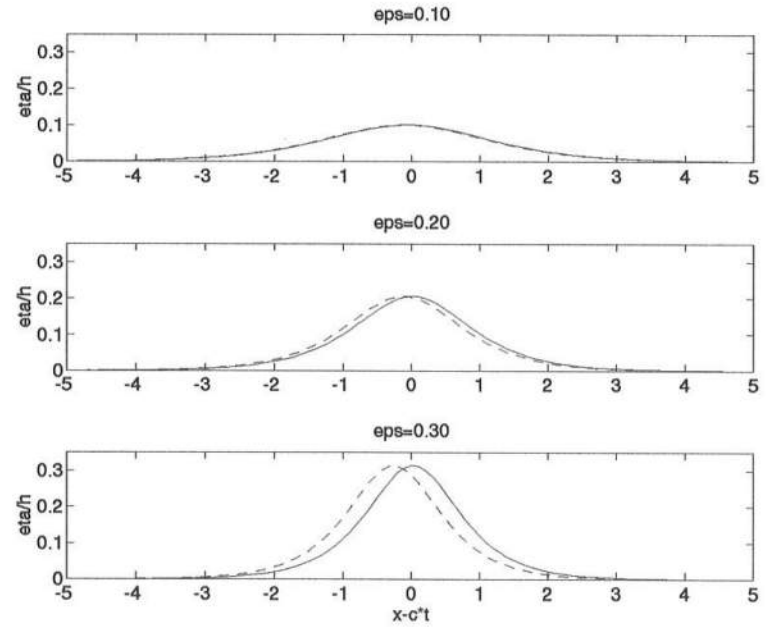

Figure 6: Comparison of solitary wave shapes at $t = 40s$ (——) and $t = 160s$ (- - -).

4.2 Solitary wave shoaling over a slope

All models in the standard Boussinesq approximation are nonlinear only to leading order, and thus are strictly valid only for relatively low waves. This assumption is necessarily violated near the wave break point, where the wave height to water depth ratio is $O(1)$. Models based on the Boussinesq approximation thus are not strictly valid in the final shoaling region and in the surf and swash zone.

In order to assess the limitations of the model in the final shoaling region, we applied it to simulate solitary wave shoaling over a slope. Numerical results are compared with a solution obtained using the boundary element method (BEM) of Grilli et al. (1989), which has been shown to be an exceptionally accurate predictor of solitary wave evolution by Grilli et al (1994). The BEM a numerical solution to Laplace's equation together with the full nonlinear surface boundary conditions, and is not limited to small water depth and weak nonlinearity.

A solitary wave with initial wave height to depth ratio of 0.2 was used for the comparison. The solitary wave was generated in a region of constant water depth and then shoaled up a slope of 1:35 before breaking. Figure 7 shows the change of the wave height to water depth ratio over distance (shown in terms of number of water depths). The dashed curve, representing the height of the BEM wave, terminates at a distance of about $26h_0$, which corresponds to the point of wave breaking. (This point was determined as being the point where the wave crest reaches a vertical asymptote.) The Boussinesq model exhibits more rapid shoaling, and also does not have any inherent behaviors that would indicate the onset of breaking. If the breaking criteria implied by the BEM solution were applied to the Boussinesq solitary wave, that wave would be judged to be breaking about one water depth further seaward than the BEM wave.

The computed wave crest speed (C_c) and the speed of center of gravity (C_g) are shown in Figure 8. The Boussinesq model is seen to slightly overpredict the crest speed of the solitary wave up until close to the break point, where the BEM crest speed increases rapidly. This feature is a result of the wave crest pitching forward in the fully nonlinear model calculation. It has been observed for some time (see, for example, Vengayil and Kirby (1986)) that Boussinesq waves do not exhibit the rapid steepening that is seen in data just prior to breaking, but instead have wave crests

that are more rounded than expected. This lack of steepening causes the Boussinesq crest position to lag behind the position predicted by BEM. In contrast, both models are seen to predict nearly equivalent values for the speed of the geometric centroid of the wave form, which is a better indicator of the overall phase speed of the waveform.

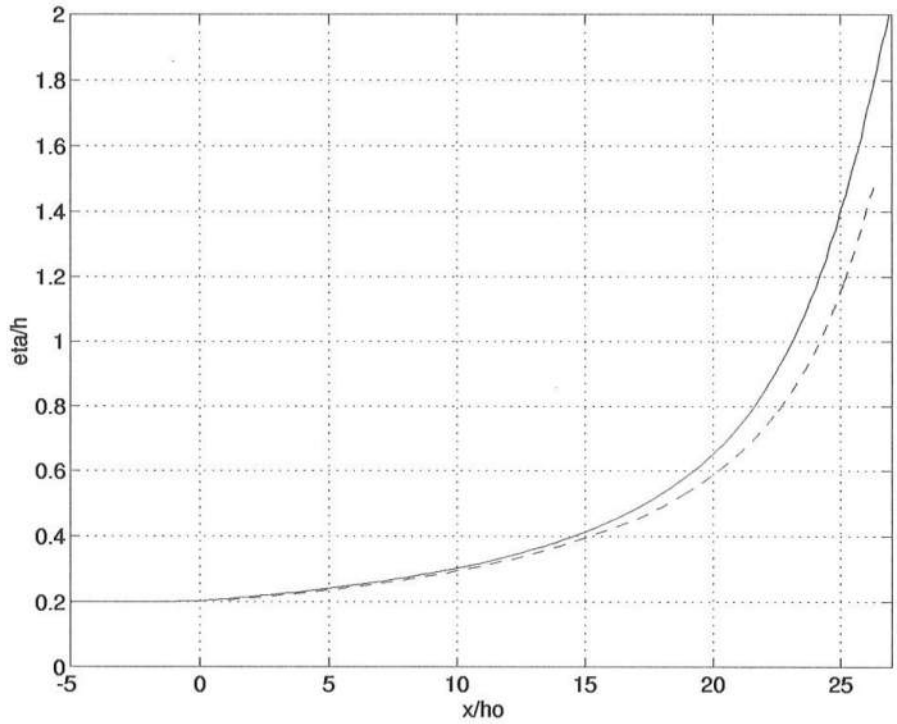

Figure 7: Comparison of solitary wave height to depth ratio over distance: Extended Boussinesq Model (——); BEM (- - -)

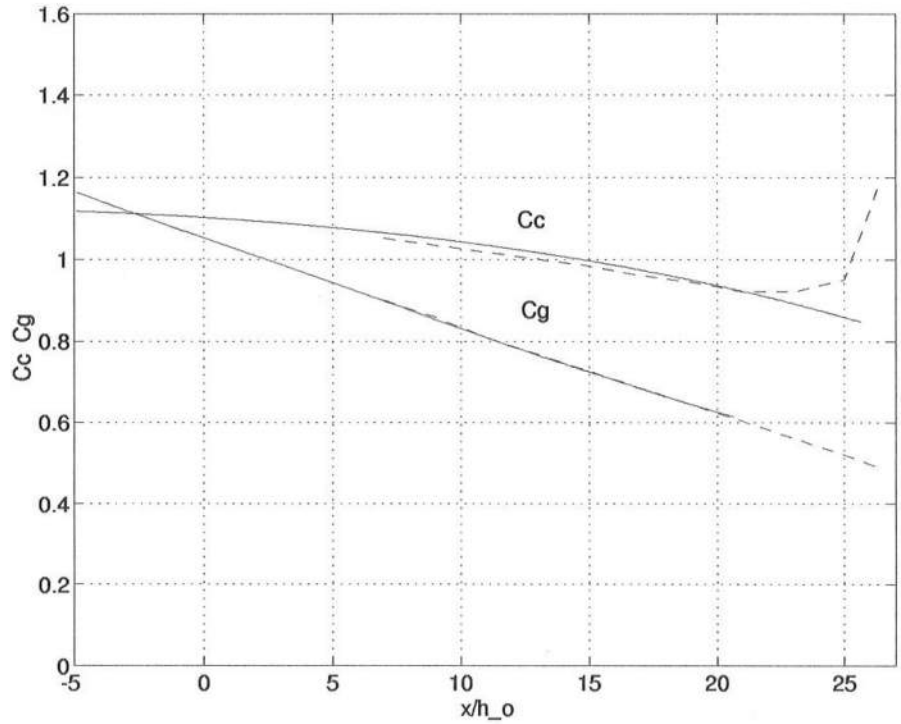

Figure 8: Comparisons of wave crest speed and speed of center of gravity over distance: Extended Boussinesq Model (——); BEM (- - -)

4.3 Solitary wave reflection from a slope

The next example addresses the reflection of solitary wave by a slope, studied by Goring (1978). The experiment layout is shown in Figure 9, where a constant slope with horizontal length L connects the left and the right ends of constant depths h_1 and h_2. A solitary wave is generated on the left and propagates to the right. Due to the presence of the slope, part of the solitary wave is reflected back to the left while the rest keeps propagating to the right, as shown in Figure 10. The time series of surface elevation at the gauge 1 are used to obtain the shapes of reflected wave, which are found to be a function of L, h_1, h_2 and the incident wave height H_I (Goring, 1978). The comparison of the shapes of measured and computed, reflected solitary waves are shown in Figure 11. In both cases, the constant water depths are $h_1 = 46.62cm$ and $h_2 = 15.54cm$, while the slope lengths L are $3.127m$ and $6.354m$, respectively. The incident wave height for both cases was $2.5cm$. The agreement between the numerical results and experimental data are essentially similar to the results of other studies (for example, Kirby and Vengayil (1988)). The discrepancy between data and model results for the case of $L = 5.354m$ is not understood at present, and may be due to the fact that the reflected wave was extremely long and low and therefore difficult to measure.

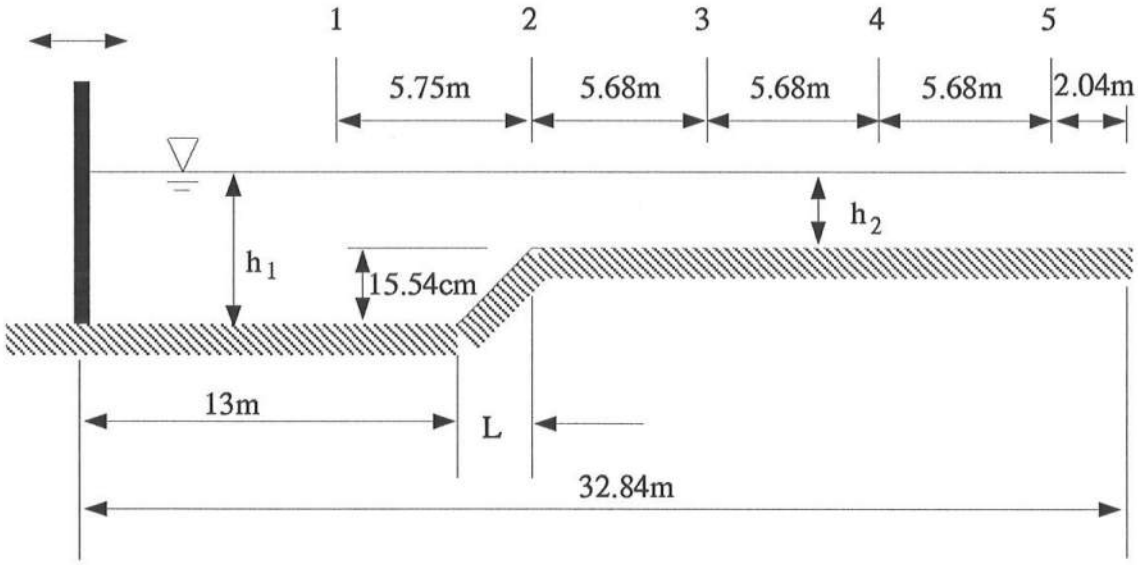

Figure 9: Experimental layout of Goring (1978)

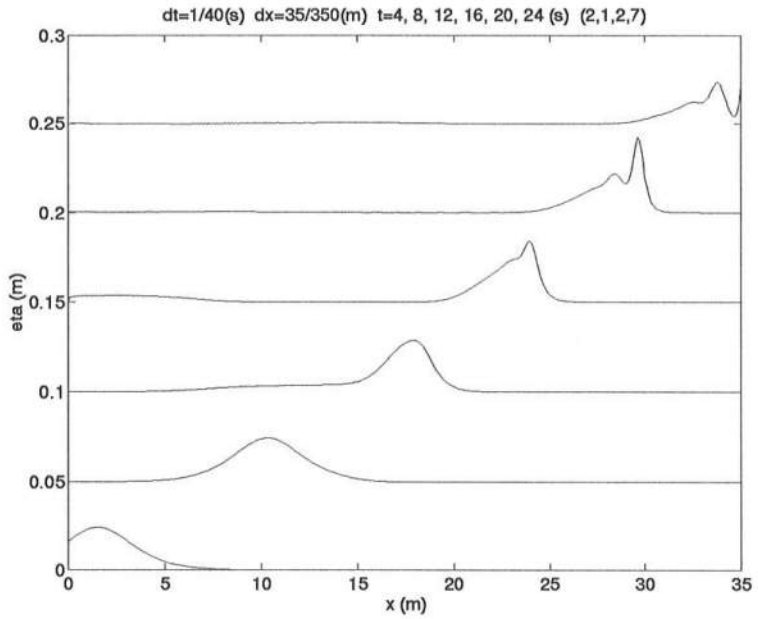

Figure 10: Spatial variations of solitary wave on a slope

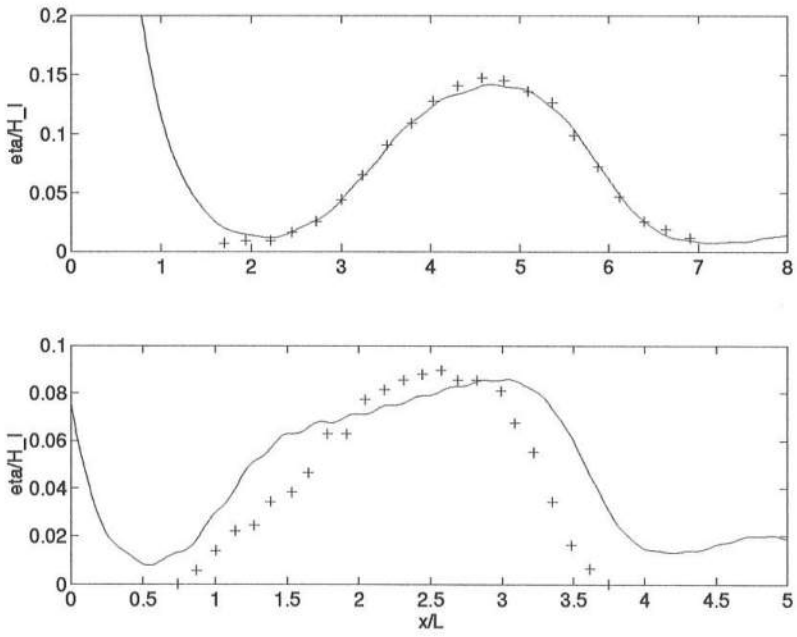

Figure 11: Comparison of reflected solitary waves: $(a)L = 3.127m$; $(b)L = 5.354m$. model (—); data (++)

4.4 Random wave shoaling on a slope

As a final example using the 1-D version of the numerical model, we study random wave propagation over a slope and compare numerical results with the laboratory data of Mase and Kirby (1992). The experimental layout is shown in Figure 12, where a constant depth of $0.47m$ on the left connects to a constant slope (1:20) on the right. Two sets of random waves with peak frequencies of $0.6Hz$ (run1) and $1.0Hz$ (run2) were generated by the wavemaker on the left. The target incident spectrum was a Pierson-Moskowitz spectrum. Wave gauges at depths $h = 47$ (two gages), $35, 30, 25, 20, 17.5, 15, 12.5, 10, 7.5, 5$ and $2.5\,cm$ collected time series of surface elevation. Further details of the experimental setup may be found in Mase and Kirby (1992).

Since no wave data is available near the wave maker, the incident boundary for the numerical model was taken to be the location of the first wave gauge $2\,m$ seaward of the toe of the beach slope (at a depth of $47cm$). The horizontal velocity u at the incident boundary was derived from the surface elevation data through Fourier analysis, based on linear relation between u and η as in (39).

The present model does not include wave breaking, which occurs in the larger waves near the gage at the depth of $17.5\,cm$. We thus end the beach slope at a point shoreward of the gage at $h = 17.5\,cm$ and introduce a flat bottom. The sponge layer method described in section 3.2 is used to absorb the waves propagating past the last gage.

Comparisons of the model and experimental data for the first 60 seconds of run1 and run2 are shown in Figure 13 and Figure 14. In each figure, results are shown for the initial conditions (bottom trace) and for gage positions $30, 25, 20$ and $17.5\,cm$ going up the plot. Both figures show that the model reproduces the measured wave form quite well. There is an apparent discrepancy in arrival time for the wave crests in run1. This error has been traced to discrepancies in time tagging of data records from separate data runs, but has not been corrected. The data for run2 shows no such discrepancy. For this case, the value of kh for the peak wave frequency is about 2.0 at the incident wave boundary, and thus this case represents a severe test of the applicability of the model to deeper water conditions. As a comparison, we ran a model based on the standard Boussinesq equations for the case of run2, and show the results in Figure 15.

In contrast to the results in Figure 14, Figure 15 shows severe discrepancies between modelled and measured waves, indicating that the standard Boussinesq model is not capable of handling the range of depths used in this example.

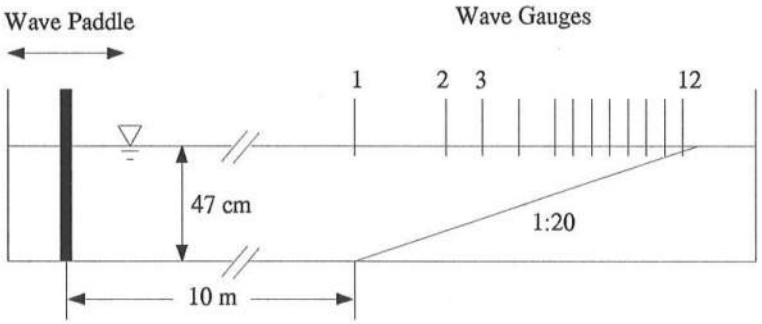

Figure 12: Experiment layout for wave shoaling experiment of Mase and Kirby (1992)

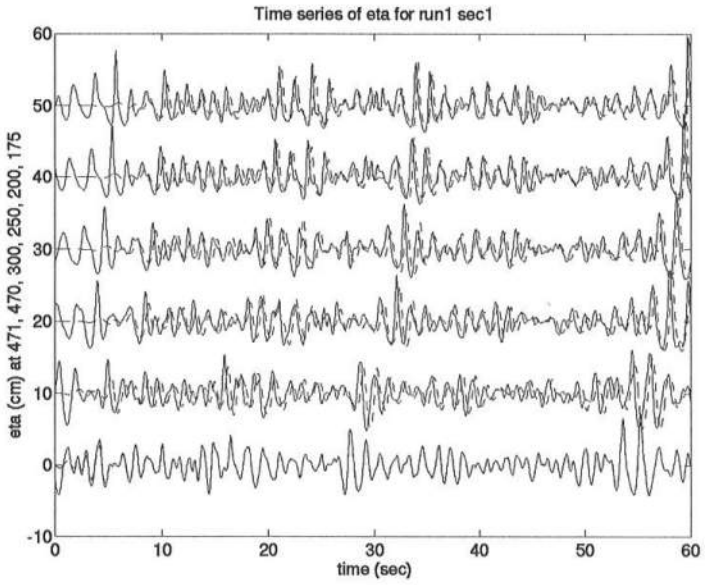

Figure 13: Comparison of time series of surface elevation for run1: model (- - -); data (——)

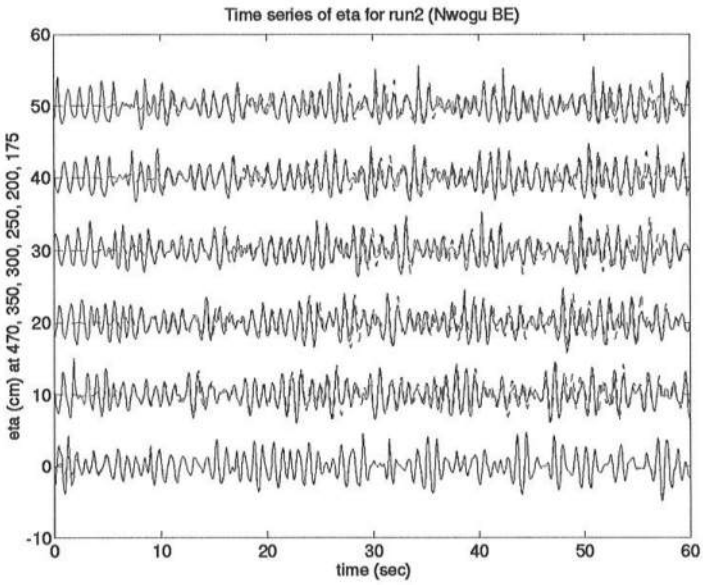

Figure 14: Comparison of time series of surface elevation for run2: model (- - -); data (——)

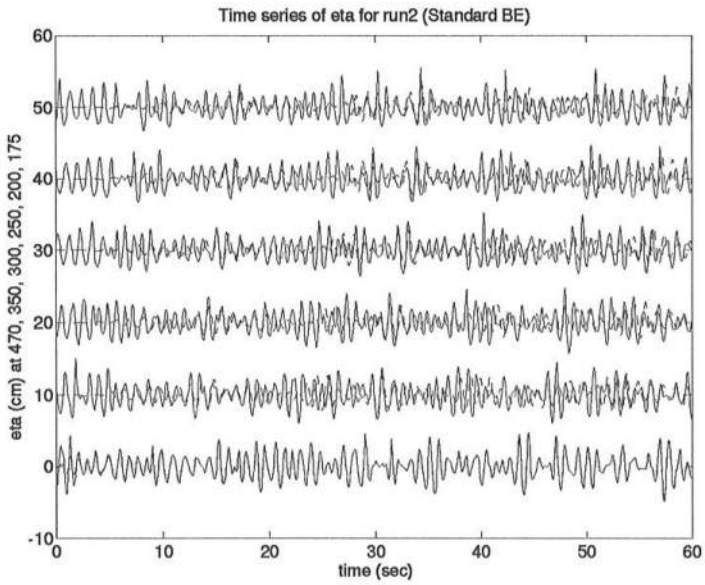

Figure 15: Comparison of time series of surface elevation for run2 using standard Boussinesq equations: model (- - -); data (——)

4.5 Wave evolution in a closed rectangular basin

Compared to the 1-D model, the 2-D model involves a number of mixed x and y derivative terms, which are handled differently in the time-stepping scheme than terms containing derivatives in one direction only. In order to verify the correctness of the model and to test its stability and associated boundary conditions in 2-D, we first use the model to study wave evolution in a closed basin of size $(L_x = 7.5\,m) \times (L_y = 7.5\,m)$. This case also gives us the opportunity to test a linearized version of the model against an analytic result, and to study the robustness of the modelled dispersion relation in a linear wave field containing a range of wave frequencies.

We consider the domain $0 \leq x \leq L_x, 0 \leq y \leq L_y$ bounded by reflective vertical walls. Within this domain, we take the initial condition to be a superelevation of the surface $\eta_0(x, y)$ above an otherwise constant depth $h_0 = 0.45m$. The linear analytic solution is obtained by first extending the domain by the method of images in both x and y directions, leading to a wave form which is periodic over $2L_x, 2L_y$ and even about any image of the reflecting sidewalls. We may then express the spatial dependence of the solution as a double cosine series, with transform coefficients determined from the initial conditions according to

$$\tilde{\eta}_{nm} = \frac{1}{(1+\delta_{n0})(1+\delta_{m0})L_x L_y} \int_{-L_x}^{L_x} \int_{-L_y}^{Ly} \eta_0(x,y) \cos(n\lambda x) \cos(m\lambda y) dx dy \tag{55}$$

where δ_{nm} denotes the Kronecker delta function, and where

$$\lambda = \frac{\pi}{L_x} = \frac{\pi}{L_y} \tag{56}$$

Each of the (n, m) modes then has a corresponding natural frequency which is given by

$$\omega_{nm}^2 = g k_{nm} \tanh(k_{nm} h_0) \tag{57}$$

where

$$k_{nm}^2 = (n\lambda)^2 + (m\lambda)^2 = \left(\frac{\pi}{L_x}\right)^2 (n^2 + m^2) \tag{58}$$

The linear solution is then given by

$$\eta(x, y, t) = \sum_{n=0}^{\infty} \sum_{m=0}^{\infty} \tilde{\eta}_{nm} \mathrm{e}^{-i\omega_{nm} t} \cos(n\lambda x) \cos(m\lambda y) \tag{59}$$

where it is understood that we are interested in the real part of the solution.

For the runs shown here, the initial surface elevation is of Gaussian shape:

$$\eta_0(x,y) = H_0 \exp\left[-2\left((x-3.75)^2 + (y-3.75)^2\right)\right] \tag{60}$$

where x and y are defined with the origin in the left and bottom corner of the basin. The initial superelevation is symmetric about the center ($x = 3.75m$, $y = 3.75m$). We show results for several maximum initial displacements.

We first consider the symmetry and conservation properties of the solution. For these examples, the initial maximum elevation H_0 is taken to be $0.045m$, with a corresponding height-to-depth ratio of 0.1. The model was run for $100s$, using a grid size of $\Delta x = 0.15m$ and time step of $\Delta t = 0.05s$. Figure 16 shows the time series of percent error in the total water volume, and surface elevations at points $(x,y) = (0m, 0m)$ and $(3.75m, 3.75m)$. In order to provide a time scale for this figure, the natural frequency of the (2,2) linear sloshing mode (which is the lowest symmetric mode relevant to the form of the initial condition) was computed and found to be $2.64s$. The computed solution shows a mix of this and higher modes, all distorted by the presence of nonlinear effects.

Since no water can escape from the basin, the water volume should remain constant with time, which is a good criterion to test the stability of the model and associated boundary conditions. Results in Figure 16 are obtained by using the combined boundary conditions (28), (37) and (38), which yield results which were more accurate than were obtained using zero normal velocity conditions and the governing equations alone. The axisymmetry of the evolving wave form about the origin of the Gaussian hill is apparent from the contour plot of surface elevation η at $t = 1s$ in Figure 17, and verifies that cross-derivative terms are being handled correctly. Figure 18 shows spatial profiles of surface elevation at time $t = 0, 20, 40, 60, 80, 100\,s$ for illustrative purposes.

Finally, we test the agreement between the linearized model and the linear solution, and show the effects of large initial nonlinearity on the computed solution. For this example, we take an initial maximum $H_0 = 0.45\,m$. This corresponds to an initial height to depth ratio of 1, which is outside the usual range of validity of the model. This ratio falls off dramatically as the initial hill of water spreads out, and the ratio typically takes on values more on the order of 0.2 during the subsequent evolution. Figure 19 shows a comparison of nonlinear (dash-dot line), linear numerical (dashed line) and linear analytical (solid line) results for the first 50 seconds after the release

of the elevation. The effect of nonlinearity is apparent through the more rapid arrival of the initial pulse at the corner point, the progressive increase in phase lead of the nonlinear crests, and in the apparent steepening of the individual nonlinear wave crests. (See, in particular, the corner point near $t = 10-15s$). There is also an apparent, but slight, discrepancy between the two linear solutions. This discrepancy shows up as an occasional modification of the shape of an individual wave crest or trough, rather than as a modification or relative drift in the overall solution. It is possible that the discrepancy is due to the effect of errors in the higher frequency portion of the solution, which contributes relatively little variance to the overall surface record. In order to test this, we computed the theoretical natural frequencies corresponding to the linearized Nwogu equation, which gives

$$\omega_{nm}^2 = g k_{nm}^2 h_0 \frac{1 - (\alpha + 1/3)(k_{nm} h_0)^2}{1 - \alpha (k_{nm} h_0)^2} \tag{61}$$

instead of (57). In Figure 20, we show the ratio of the Boussinesq natural frequency to the exact natural frequency over the range of mode numbers which are represented in the analytic and numerical solutions. The ratio dips slightly below 1 for n, m values below about 10 and then rises gradually. The first 10 modes in each direction account for essentially all of the variance in the solution, and the errors in the ratio are less than 1% in this range. For contrast, we show the frequency ratios corresponding to the standard Boussinesq model in Figure 21. Errors on the order of 5% are seen for (m, n) pairs in the range of energetic modes, indicating that the present example should also show sizeable errors if run using the standard Boussinesq approximation.

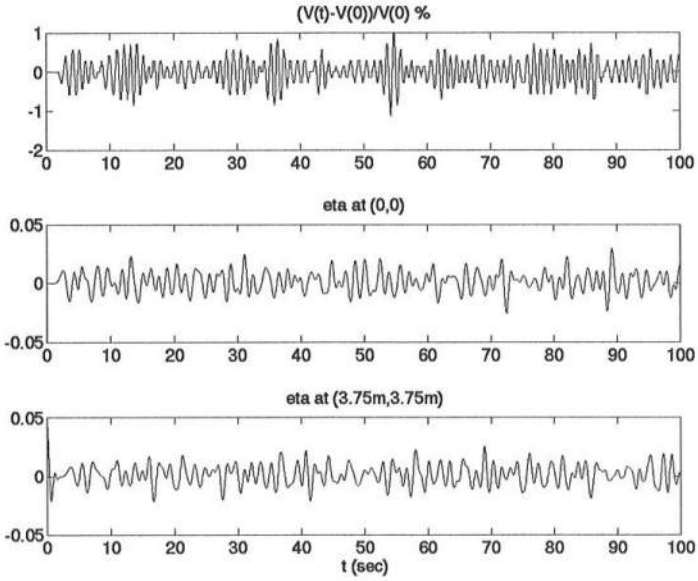

Figure 16: Time series of surface elevations and overall water volume for wave in rectangular box, $H_0 = 0.045\,m$.

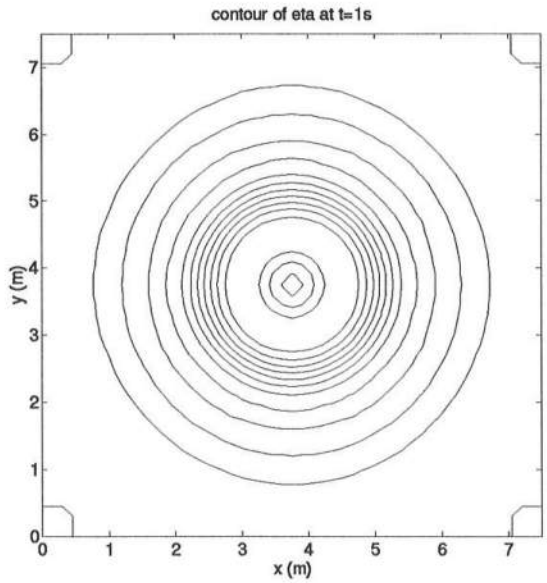

Figure 17: Contour of η at $t = 1\,s$, illustrating rotational symmetry of the evolving cylindrical wave.

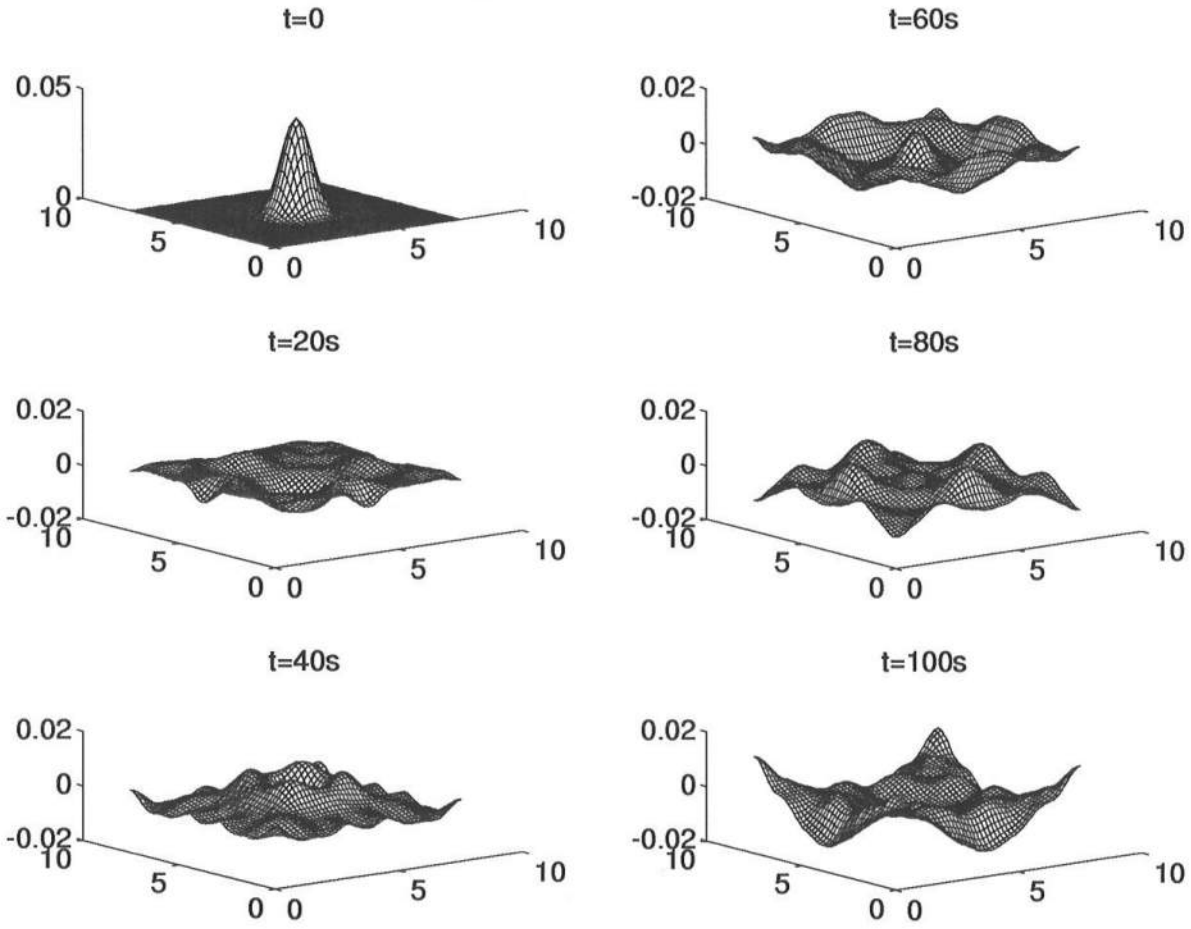

Figure 18: Spatial profiles of surface elevation.

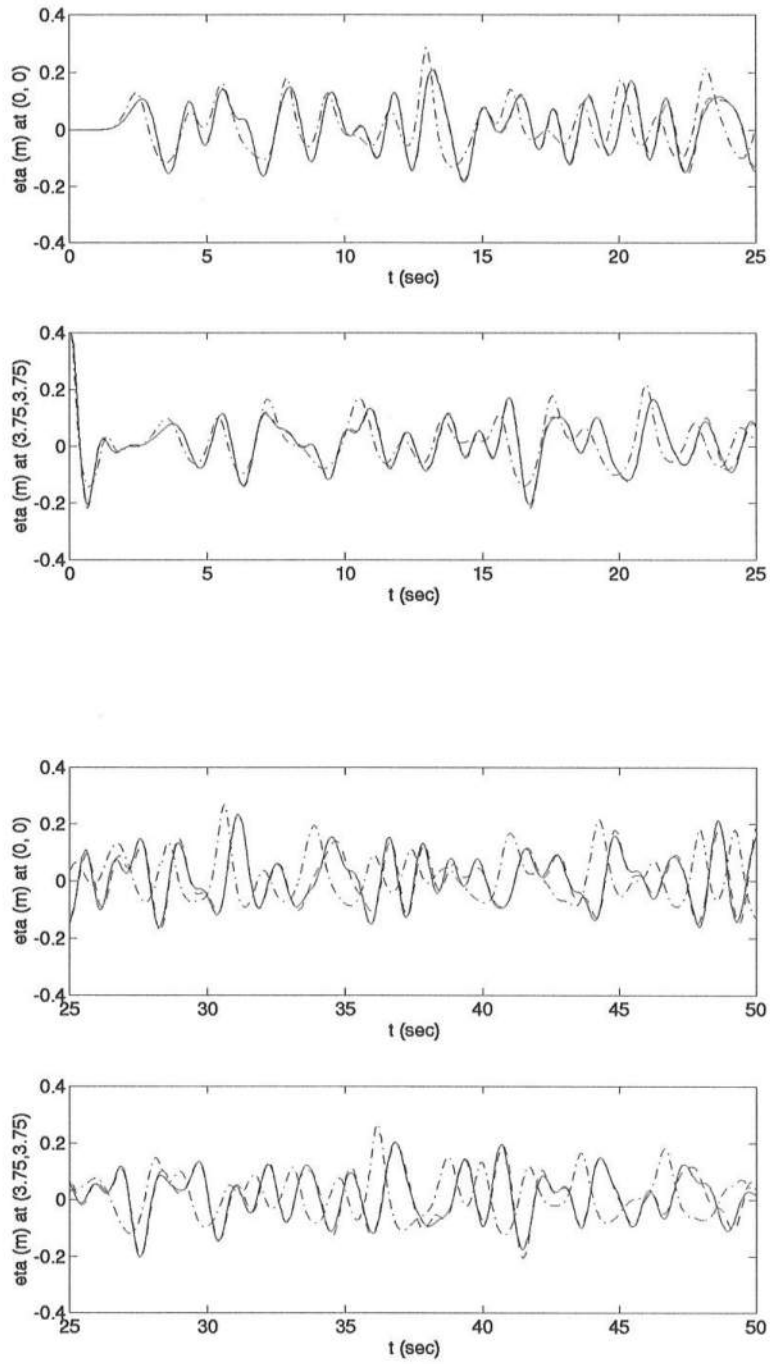

Figure 19: Comparison of solutions for initial Gaussian elevation in square box. Nonlinear (dash-dot line), linear numerical (dashed line) and linear analytical (solid line) solutions.

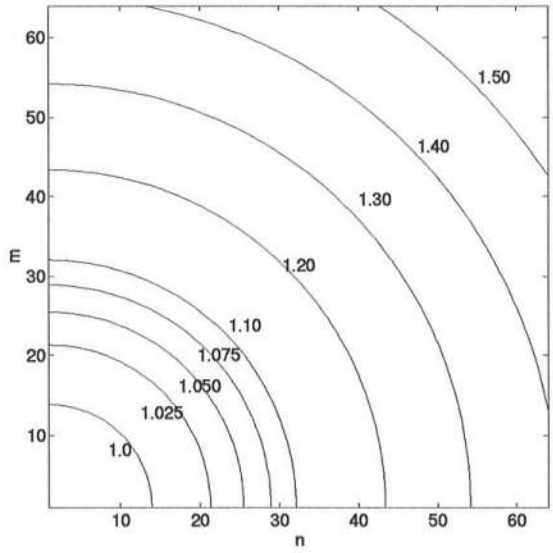

Figure 20: Ratio of Extended Bousinesq natural frequencies to exact natural frequencies for the range of mode numbers considered in the analytic and numerical solution.

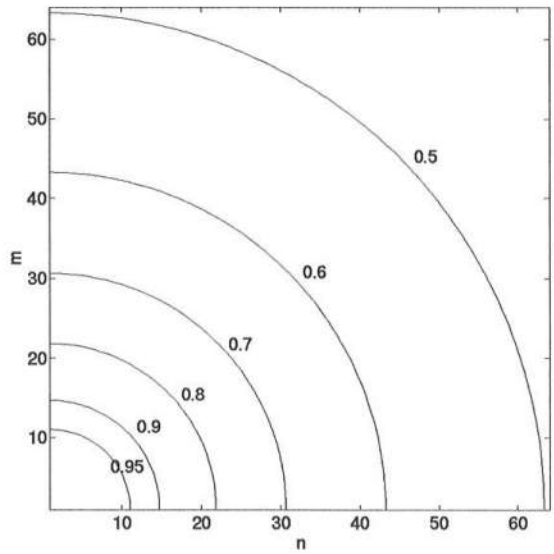

Figure 21: Ratio of standard Bousinesq natural frequencies to exact natural frequencies for the range of mode numbers considered in the analytic and numerical solution.

4.6 Monochromatic wave propagation over a shoal

We now apply the 2-D version of the numerical model to study monochromatic wave propagation over a shoal. The geometry used corresponds to the experimental arrangement of Berkhoff et al. (1982). This experiment remains a standard test for verifying models based on the mild slope equation. See, for example, Kirby and Dalrymple (1984) and Panchang and Kopriva (1989). The standard form of Boussinesq equations is not appropriate in this situation due to the relatively deep water conditions used. The value of kh at the wavemaker in this example is about 1.9, making the example similar in severity to the run2 example in section 4.4.

The experimental geometry and location of measurement transects is shown schematically in Figure 22. Monochromatic waves with period $1s$ and amplitude $2.32cm$ are generated by a wavemaker at $x = -10m$. The remaining computational domain includes two side walls (which are located at $y = -10m$ and $y = 10m$) and an absorbing boundary at $x = 12\,m$. The bottom bathymetry consists of an elliptic shoal resting on a plane beach with a constant slope of (1:50). Bottom contours on the slope are oriented at an angle of 20° to the y - axis. Further details of the geometry may be obtained in Berkhoff et al (1982) or Kirby and Dalrymple (1984).

Wave heights along eight sections near the shoal were measured in the experiment. Figure 23 shows the comparisons of the model results and experiment data. Agreement is generally good, but not as good as seen using models based on third-order Stokes wave dispersion (Kirby and Dalrymple, 1984). The present model predicts a somewhat lower and broader central focus region, indicating that the effects of nonlinearity in intermediate water depths are somewhat exaggerated, although not by an amount that damages the overall quality of the prediction. The level of agreement seen here indicates that the new form of Boussinesq equations may be used with some confidence in intermediate water depths, but that some effort should be put into obtaining formulations that produce a more correct level of nonlinear effects.

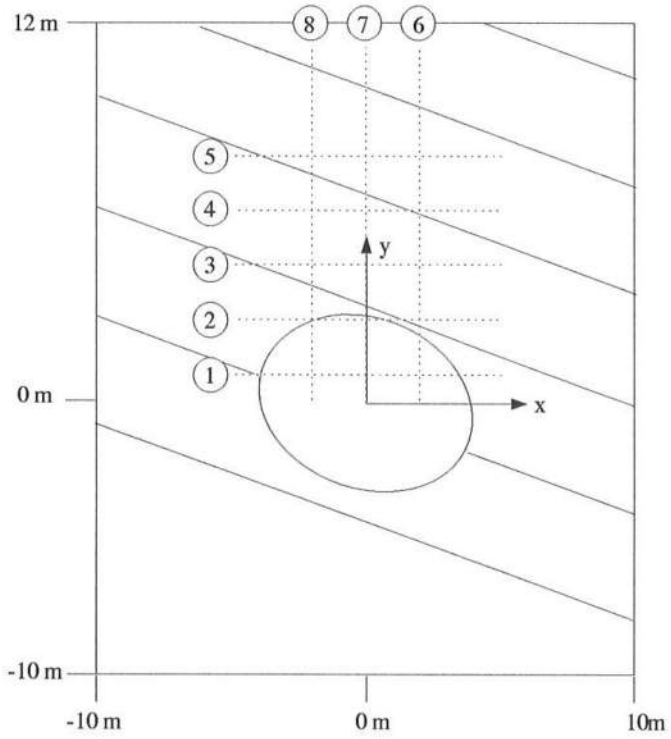

Figure 22: Experiment layout for wave focussing experiment of Berkhoff et al. (1982)

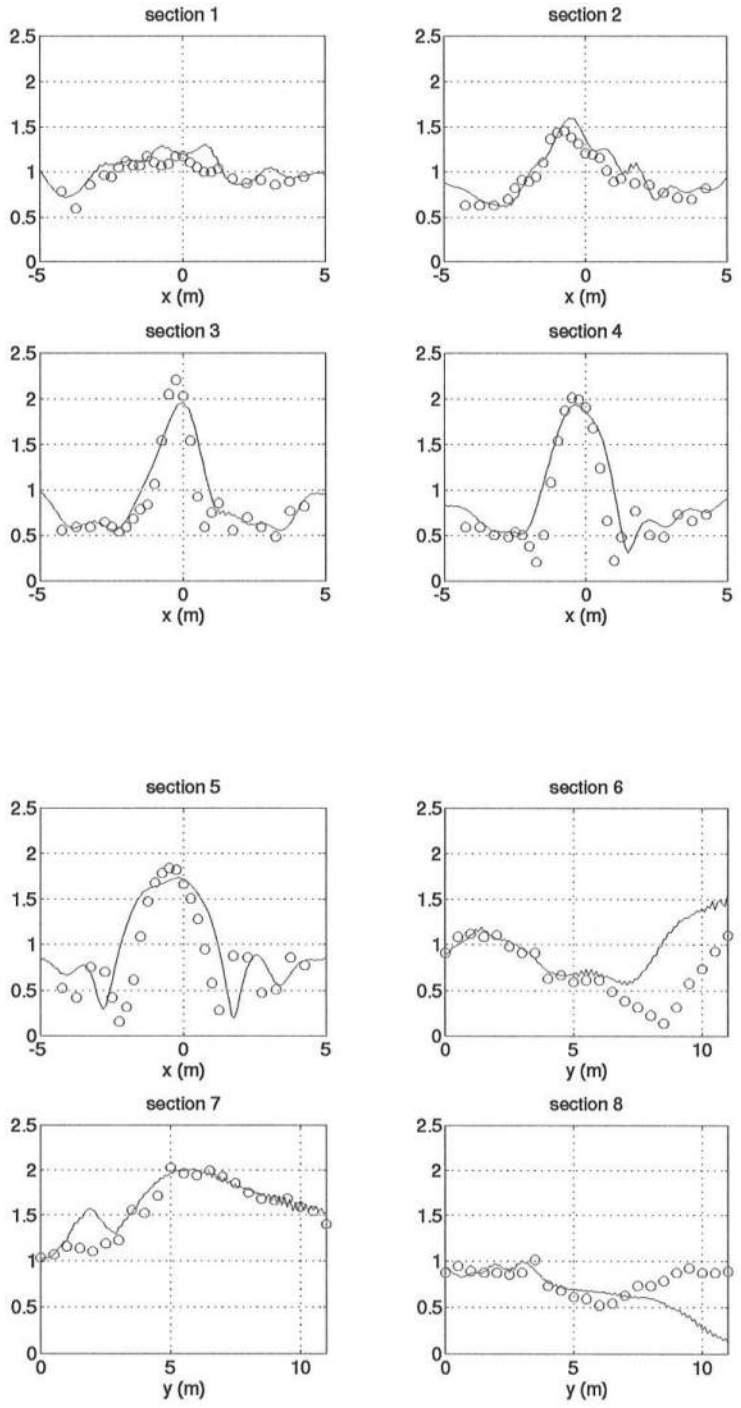

Figure 23: Comparison of numerical results (—) and experimental data (oo) for waveheights on measuring transects of Berkhoff et al (1982).

4.7 Mach reflection of Cnoidal waves

As a final example, we study the Mach-stem resulting from the grazing-angle reflection of a cnoidal wave by a wall. First, for a given wave period T, wave height H and water depth h, a permanent form solution corresponding to a cnoidal wave is obtained numerically by solving a system of nonlinear equations obtained from a frequency domain decomposition of Nwogu's equations (Kaihatu, 1993). The results are then used as the incident wave boundary condition for the numerical model. Figure 24 shows the experimental layout of Hammack et al. (1990), where cnoidal waves with direction θ were generated at $x = 0$. Two side walls are located at $y = 0$ and $y = -13.25m$. The wave period is $T = 1.4785s$, wave height $H = 5.366cm$, and water depth $h = 20cm$. Time series of water surface elevation are obtained by two wave gauge arrays which are parallel $(\#18, 17, 16, 15, 14, 13, 5)$ and perpendicular $(\#13, 9, 8, 7, 6, 4, 3, 2, 1)$ to the $y = 0$ side wall. Six sets of data were collected, corresponding to different θ values. Here we present the comparison of model and experiment results for case 1 with minimum θ $(10.13°)$ and case 6 with maximum θ $(44.32°)$. Further details of incident wave conditions may be found in Kirby (1990)

Figures 25 and 26 show results for the smallest angle. In Figure 25, the waves are seen to be in phase over the first four gages perpendicular to the wall, which indicates the width of the Mach stem region. Beyond the fourth gage, the waves are apparently incident towards the wall with a small angle of approach. Agreement between measured and computed wave forms is good both inside and outside the stem region.

Figures 27 and 28 show results for the largest angle of incidence, where the reflection pattern is essentially regular. Figure 27 shows what is essentially a simple short-crested wave pattern, where the individual wave crests have been steepened by nonlinearity. The agreement between model and experiment is again good.

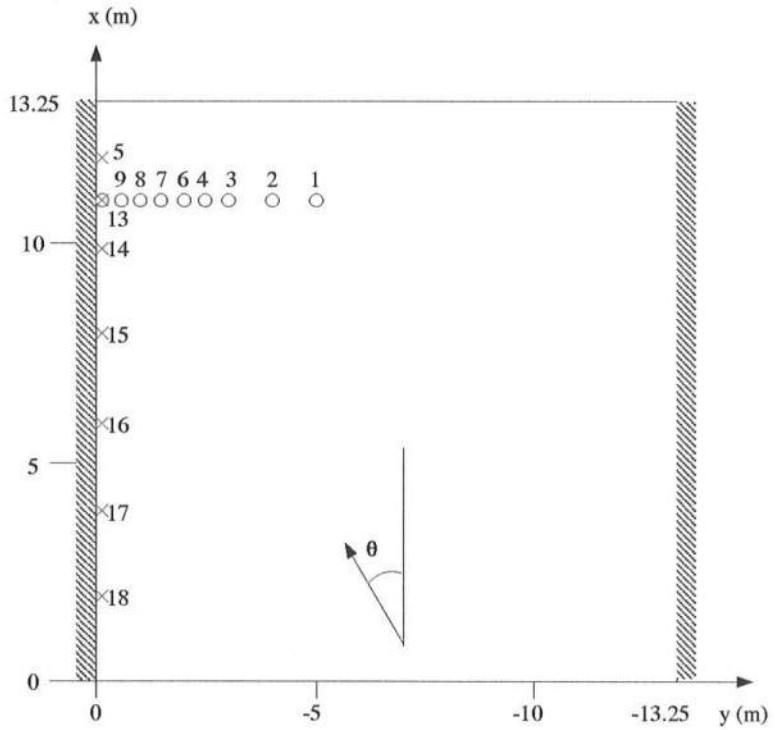

Figure 24: Experimental layout for an experiment on Mach reflection of cnoidal waves (Hammack et al., 1990).

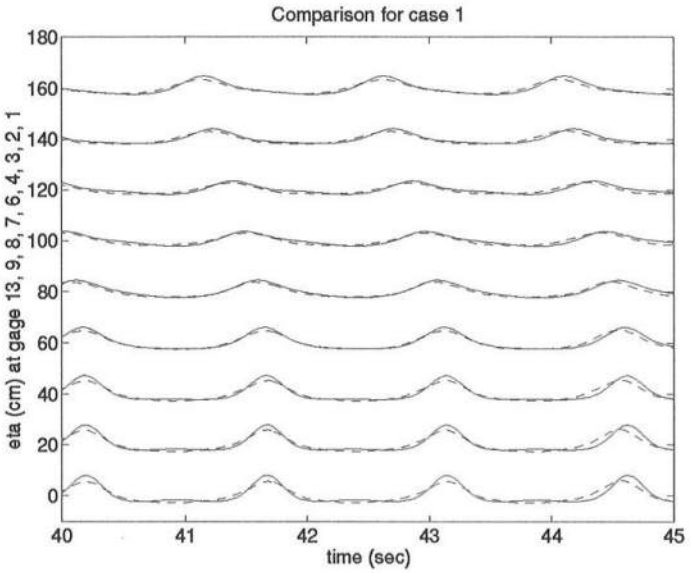

Figure 25: Comparison of numerical (---) and experimental data (——) for case 1. Gages perpendicular to wall.

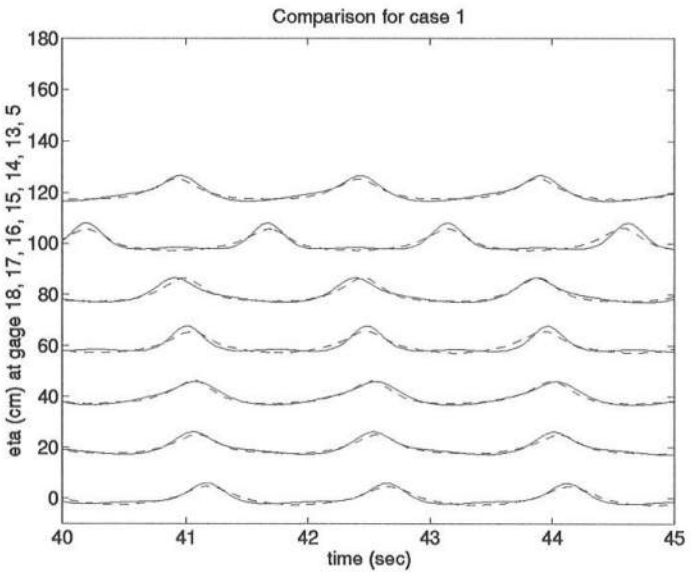

Figure 26: Comparison of numerical (---) and experimental data (——) for case 1. Gages parallel to wall.

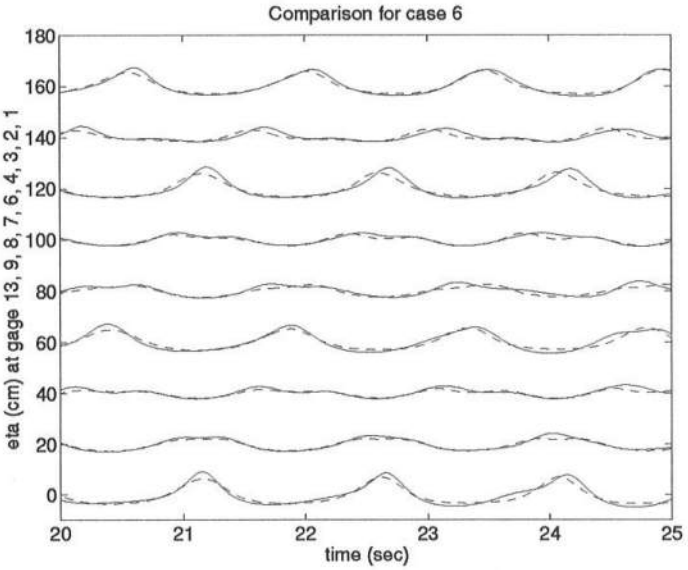

Figure 27: Comparison of numerical (- - -) and experimental data (——) for case 6. Gages perpendicular to wall.

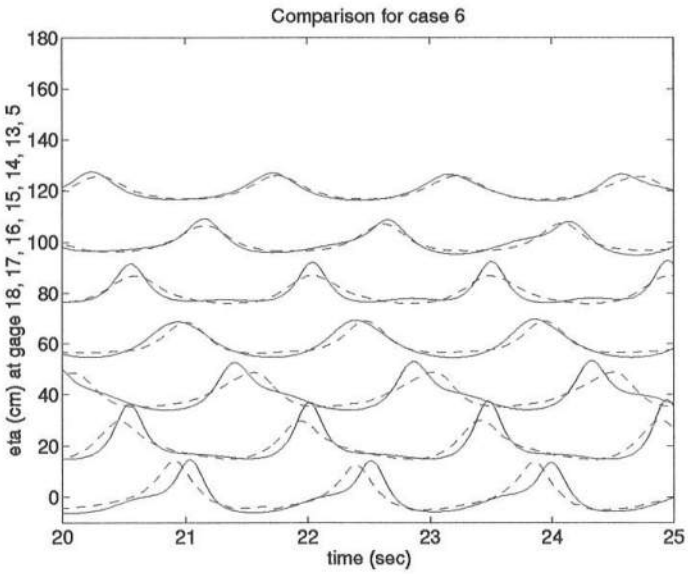

Figure 28: Comparison of numerical (- - -) and experimental data (——) for case 6. Gages parallel to wall.

5 Conclusion

A high order numerical scheme has been developed for a new form of the Boussinesq equations derived by Nwogu (1993). The scheme has been tested in a number of examples which illustrate its basic stability and which show that the new Boussinesq equations may be applied to a wide range of water depths.

Two of the examples studied above point out cases where there are discrepancies between nonlinear effects in the Boussinesq approximation and corresponding effects in data or in alternate analytical formulations. In both cases, these limitations are likely manifestations of the lowest order nature of the model, which does not correctly represent either the $O(1)$ nonlinearity of waves near breaking or the dominant cubic nonlinearity of intermediate depth waves. For this reason, we are presently extending the model equations described here to include higher order terms; results for this extension of the model capability will be described separately (Kirby and Wei, 1994).

Appendix: Solitary Wave Solution for Extended Boussinesq Model

For convenience, we rewrite Nwogu's equations for 1-D horizontal flow in constant depth

$$\eta_t + u_x + (\eta u)_x + (\alpha + 1/3)h^3 u_{xxx} = 0 \quad \text{(A1)}$$

$$u_t + \eta_x + u u_x + \alpha h^2 u_{xxt} = 0 \quad \text{(A2)}$$

where

$$\alpha = \frac{1}{2}\left(\frac{z_\alpha}{h}\right) + \frac{z_\alpha}{h} \quad \text{(A3)}$$

Instead of the velocity u, we use the velocity potential ϕ (such that $u = \phi_x$) as a variable. Then equations (A1) and (A2) become

$$\eta_t + \phi_{xx} + (\eta\phi_x)_x + (\alpha + 1/3)h^3 \phi_{xxxx} = 0 \quad \text{(A4)}$$

$$\phi_t + \eta + \frac{1}{2}(\phi_x)^2 + \alpha h^2 \phi_{xxt} = 0 \quad \text{(A5)}$$

Substituting η from (A5) into (A4) and retaining terms which are consistent with the ordering in the Boussinesq equations, we have

$$-\phi_{tt} + gh\phi_{xx} - 2\phi_x\phi_{xt} - \phi_t\phi_{xx} + gh^3(\alpha + 1/3)\phi_{xxxx} - \alpha h^2\phi_{xxtt} = 0 \tag{A6}$$

The truncation in the last step is responsible for the fact that the analytic solitary waves differ by a small amount from their numerical counterparts, even in the limit of small step size. Equation (A6) is transformed into an ordinary differential equation by introducing $\xi = x - Ct$ (thus $\phi_x = \phi'$ and $\phi_t = -C\phi'$)

$$(gh - C^2)\phi'' + 3C\phi'\phi'' + [(\alpha + 1/3)gh^3 - \alpha h^2C^2]\phi'''' = 0 \tag{A7}$$

Integrating the above equation once results in

$$(gh - C^2)\phi' + \frac{3}{2}C(\phi')^2 + [(\alpha + 1/3)gh^3 - \alpha h^2C^2]\phi''' = G_1 \tag{A8}$$

Multiplying (A8) by $2\phi''$ and integrating again yields

$$(gh - C^2)(\phi')^2 + C(\phi')^3 + [(\alpha + 1/3)gh^3 - \alpha h^2C^2](\phi'')^2 = 2G_1\phi' + G_2 \tag{A9}$$

The integration constants G_1 and G_2 are zero for solitary waves since $\phi = \phi' = \phi'' = \phi''' = 0$ as $\xi \to \infty$. Assume the solution form of ϕ' to be

$$\phi' = A\text{sech}^2(B\xi) \tag{A10}$$

Substituting (A10) into (A9) yields

$$A = \frac{C^2 - gh}{C} \tag{A11}$$

$$B^2 = \frac{C^2 - gh}{4[(\alpha + 1/3)gh^3 - \alpha h^2C^2]} \tag{A12}$$

From (A5), we have

$$\eta = A_1\text{sech}^2(B\xi) + A_2\text{sech}^4(B\xi) \tag{A13}$$

where

$$A_1 = \frac{C^2 - gh}{3[(\alpha + 1/3)gh - \alpha C^2]}h \tag{A14}$$

$$A_2 = -\frac{(C^2 - gh)^2}{2ghC^2}\frac{[(\alpha + 1/3)gh + 2\alpha C^2]}{[(\alpha + 1/3)gh - \alpha C^2]}h \tag{A15}$$

From the boundary condition $\eta = a$ at $\xi = 0$, we have

$$\frac{C^2 - gh}{3[(\alpha + 1/3)gh - \alpha C^2]}h - \frac{(C^2 - gh)^2}{2ghC^2}\frac{[(\alpha + 1/3)gh + 2\alpha C^2]}{[(\alpha + 1/3)gh - \alpha C^2]}h = a \qquad \text{(A16)}$$

which can be rearranged as (with $\varepsilon = a/h$)

$$2\alpha(\frac{C^2}{gh})^3 - (3\alpha + 1/3 + 2\alpha\varepsilon)(\frac{C^2}{gh})^2 + 2\varepsilon(\alpha + 1/3)(\frac{C^2}{gh}) + \alpha + 1/3 = 0 \qquad \text{(A17)}$$

Acknowledgement

This research was supported by the Army Research Office through University Research Initiative grant DAAL 03-92-G-0116.

References

Abbott, M. B., McCowan, A. D. and Warren, I. R., 1984, "Accuracy of short-wave numerical model", *J. Hydr. Engnrg.*, **110**, 1287-1301.

Berkhoff, J. C. W., Booy, N. and Radder, A. C., 1982, "Verification of numerical wave propagation models for simple harmonic linear water waves", *Coastal Engng*, **6**, 255-279.

Elgar, S. and Guza, R. T., 1985, "Shoaling gravity waves: comparisons between field observations, linear theory and a nonlinear model", *J. Fluid Mech.*, **158**, 47-70.

Elgar, S. and Guza, R. T., 1986, "Nonlinear model predictions of bispectra of shoaling surface gravity waves", *J. Fluid Mech.*, **167**, 1-18.

Elgar, S., Freilich, M. H. and Guza, R. T., 1990, "Model-data comparisons of moments of nonbreaking shoaling surface gravity waves", *J. Geophys. Res.*, **95**(C9), 16055-16063.

Engquist, B. and Majda, A., 1977, "Absorbing boundary conditions for the numerical simulation of waves", *Math. Comp.*, **31**, 629-65.

Freilich, M. H., and Guza, R. T., 1984, "Nonlinear effects on shoaling surface gravity waves", *Philos. Trans. R. Soc. London, Ser. A*, **311**, 1-41.

Freilich, M. H., Guza, R. T., and Elgar, S. L., 1993, "Field test of two-dimensional Boussinesq shoaling wave model", *MEET'N'93– First Joint ASCE/ASME/SES MEETING*, Eds: C.T. Herakovich and J.M. Duva, Charlottesville, VA, USA (abstract only).

Grilli, S., Skourup, J., and Svendsen, I. A., 1989, "An efficient boundary element method for nonlinear water waves", *Engineering Analysis with Boundary Elements*, **6**, 2, 97-107.

Grilli, S. T., Subramanya, R., Svendsen, I. A. and Veeramony, J., 1994, "Shoaling of solitary waves on plane beaches", submitted to *J. Waterway, Port, Coastal and Ocean Engrng.*

Goring, D. G., 1978, "Tsunamis–the propagation of long waves onto a shelf". Ph.D dissertation, California Institute of Technology, Pasadena, California.

Hammack, J. L., Scheffner, N. W., and Segur, H., 1990, personal communication.

Israeli, M. and Orszag, S. A., 1981, "Approximation of radiation boundary conditions", *J. Comp. Phys.*, **41**, 115-13.

Kaihatu, J. M., 1993, personal communication.

Kirby, J. T., 1990, "Modelling shoaling directional wave spectra in shallow water", *Proc. of 22nd Int. Conf. Coastal Engr.*, Delft, 109-121.

Kirby, J. T. and Dalrymple, R. A., 1984, "Verification of a parabolic equation for propagation of weakly-nonlinear waves", *Coastal Engng*, **8**, 219-232.

Kirby, J. T. and Vengayil, P., 1988, "Nonresonant and resonant reflection of long waves in varying channels", *J. Geophys. Res.*, **93**, 10782-10796.

Kirby, J. T. and Wei, G., 1994, "Derivation and properties of a fully nonlinear model for weakly dispersive surface waves", in preparation.

Larsen, J. and Dancy, H., 1983, "Open boundaries in short-wave simulations - A new approach", *Coastal Engrng.*, **7**, 285-297.

Liu P. L-F., Yoon, S. B. and Kirby, J. T., 1985, "Nonlinear refraction-diffraction of waves in shallow water", *J. Fluid Mech.*, **153**, 185-201.

Madsen, P. A., Murray, R. and Sørensen, O.R., 1991, "A new form of Boussinesq equations with improved linear dispersion characteristics", *Coastal Engng*, **15**, 371-388.

Mase, H. and Kirby, J. T., 1992, "Hybrid frequency-domain KdV equation for random wave transformation", *Proc. 23rd Int. Conf. Coastal Engr.*, Venice, Oct. 1992.

Murray, R. J., 1989, "Short wave modelling using new equations of Boussinesq type", *Proc. 9th Australasian Conference on Coastal and Ocean Engineering*, Adelaide, Australia, 331-336.

Nwogu, O., 1993, "An alternative form of the Boussinesq equations for nearshore wave propagation", *J. Waterway, Port, Coast. Ocean Engng*, **119**(6), 618-638.

Panchang, V. G. and Kopriva, D. A., 1989, "Solution of two-dimensional water-wave propagation problems by Chebyshev collocation", *Mathl Comput. Modelling*, Vol. **12**, No. 6, 625-640.

Peregrine, D. H., 1967, "Long waves on a beach", *J. Fluid Mech.*, **27**, 815-82.

Rygg, O. B., 1988, "Nonlinear refraction-diffraction of surface waves in intermediate and shallow water", *Coastal Engng*, **12**, 191-211.

Schember, H. R., 1982, "A new model for three-dimensional nonlinear dispersive long waves", Ph.D dissertation, California Institute of Technology, Pasadena, California.

Vengayil, P. and Kirby, J. T., 1986, "Shoaling and reflection of nonlinear shallow water waves", *Proc. 20th Intl. Conf. Coast. Engrng.*, Taipei, 794-806.

Whalin, R. W., 1971, "The limit of applicability of linear wave refraction theory in a convergence zone", Res. Rept. H-71-3, Hydraulics Laboratory, U. S. Army Corps of Engineers Waterways Experiment Station, Vicksburg.

Witting, J. M., 1984, "A unified model for the evolution of nonlinear water waves", *J. Comp. Phys.*, **56**, 203-239.